Quark Physics Laboratory Graduate School of Advanced Science and Engineering Physics Program

Master thesis

Charged-Particle Multiplicity Dependence of J/ψ Yield and ρ+ω Mass Width via Dimuon Measurement in p-p collisions at $\sqrt{s} = 13.6$ TeV as Potential Signatures of Quark-Gluon Plasma Production in Small Collision Systems

Auther: Tomo Ito

Supervisor: Prof. Kenta Shigaki
Chief examiner: Prof. Kenta Shigaki
Examiner: Prof. Tomohiro Inagaki
Examiner: Program-Specific Prof. Toru Takahashi

Abstract

In the early microseconds after the Big Bang, the state of the universe is expected to be high temperature and density called Quark-Gluon Plasma (QGP) formed with quark confinement breaking. Using the Large Hadron Collider (LHC) at the European Organization for Nuclear Research (CERN), The QGP is observed successfully with heavy-ion collisions. However, evidence for QGP generation in small collision systems, such as p-p and p-Pb collisions, has not been obtained. In this study, I anticipate QGP generation in high-multiplicity collision events. Some measurements of phenomena at high charged-particle multiplicity in p-Pb collisions show similar behavior to results measured by Pb-Pb collisions. This study discusses the charged-particle multiplicity dependence of J/ψ production and the $\rho+\omega$ mass width with ALICE which is one of the experiments in CERN. Additionally, discussions of the results from the ϕ meson measurement are also included. Individual extraction of ρ and ω is not easy due to the close masses. Therefore, this study approximates them as a combined signal $\rho + \omega$. The J/ψ production serves as a probe for QGP generation. J/ψ production is suppressed in QGP via color screening and observed in Pb-Pb collisions. I anticipate that the $\rho + \omega$ mass width reflects the phenomenon of spontaneous chiral symmetry breaking recovery near the QGP phase transition temperature.

This study uses proton-proton collision events at the center-of-mass energy of 13.6 TeV from the year 2022. To improve the resolution of track reconstruction, The new tracking chamber is introduced. J/ψ, ρ, ω, and ϕ are detected in forward($-3.6 \leq \eta \leq -2.45$). The charged-particle multiplicity is measured in central($|\eta| \leq 1.22$).

In this study, charged-particle multiplicity dependence of the yield, width and mean mass of J/ψ, $\rho + \omega$, and ϕ are measured with the new data acquired in 2022. As a result, the dependence of self-normalized J/ψ yield on charged-particle multiplicity shows strange behavior at low charged-particle multiplicity. I expect the cause is due to accuracy of charged-particle multiplicity measurement. The mass width of $\rho + \omega$ and ϕ as a function of charged-particle multiplicity show weak dependence of charged-particle multiplicity. The mass width of $\rho + \omega$ and ϕ is higher than PDG values by a factor of 2 for $\rho + \omega$ compared with PDG of ω and 4 for PDG of ϕ due to detector resolution. The ρ mass width in PDG is so high that can be seen

if $\rho + \omega$ is separated independently. In case quality of track reconstruction improves more, the mass width of ω and ϕ can be also observed.

Contents

List of Figures

Chapter 1

Introduction

1.1 QCD

All interactions including strong interaction are described by quantum field theory. Electromagnetic interaction is described by quantum electrodynamics (QED), and quantum chromodynamics (QCD) which explain strong interaction based on QED. Interaction is carried by gauge boson corresponding to the field. Interaction between particles and field is described via Lagrangian. In case Lagrangian is invariant after gauge transformation, Lagrangian has gauge symmetry. All interactions require Lagrangian to have gauge symmetry. Gauge transformation is as follows.

$$\psi_f \to e^{iQ_f\theta(x)}\psi_f \tag{1.1}$$

$$A_\mu \to A_\mu + \frac{1}{e}\partial_\mu\theta(x) \tag{1.2}$$

Based on these principals, QED Lagrangian is given by

$$\mathcal{L}_{QED} = \bar{\psi}_f(i\gamma^\mu\partial_\mu - m_f)\psi_f + eQ_f\bar{\psi}_f\gamma^\mu\psi_f A_\mu - \frac{1}{4}F_{\mu\nu}F^{\mu\nu} \tag{1.3}$$

The first term shows free particles, which are not interacted by the field. The second term describes the interaction between the charged particle and the electromagnetic field. The third term means electromagnetic field.

Gauge bosons propagating strong interactions are gluons. Strong interactions work on color-charged particles. The color charge has three degrees of freedom (red, blue, and green). QCD is constructed on the condition that the

color's internal degrees of freedom are localized by rotation of them. QCD is an SU(3) gauge theory, as the 3×3 unitary matrix represents this rotational transformation. QCD lagrangian is as follows

$$\mathcal{L}_{QCD} = \bar{\psi}_{q,a}(i\gamma^{\mu}\partial_{\mu} - m_q)\psi_f + g_s\bar{\psi}_{q.a}\gamma^{\mu}T^A_{ab}\psi_{q,b}G^A_{\mu} - \frac{1}{4}G^A_{\mu\nu}G^{A\mu\nu} \qquad (1.4)$$

The first term shows free quark. The second term describes the interaction between quarks and gluon field. The third term means gluons. Each term is similar to those of QED, but the interaction between gluons described in the third term is a unique feature of QCD. As electromagnetic interaction works on charged-particle, photons that is gauge boson of electromagnetic interaction don't interact with photons. However, gluons have color.

In QCD, the coupling constant depends on the momentum shift scale Q^2 due to the renormalization process. In QED and QCD, divergence occurs in higher-order calculation and this is called 'Ultraviolet divergence'. This divergence is removed by the renormalization process. The renormalization process is determined by the renormalization scale μ which is the free parameter of momentum. Momentum shift scale Q^2 is used as a renormalization scale in general. As a result, the coupling constant depends on the momentum shift scale Q^2. The coupling constant as a function of Q^2 is measured and agreed with theoretical calculation. (Fig 1.1)
This result means that the higher Q^2 becomes, the weaker strong interaction becomes. This phenomenon is called 'Asymptotic freedom'. The high Q^2 interaction is called the hard process and the soft process is low Q^2. Perturbative QCD can calculate hard processes. Lattice QCD can describe the soft process.

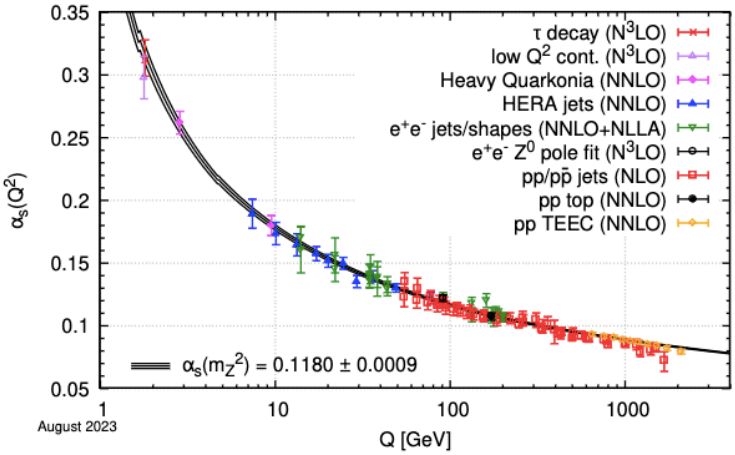

Figure 1.1: Coupling constant with dependence of momentum shift scale (Q^2).[1]

The potential between a quark and an anti-quark is calculated by lattice QCD(Fig 1.2). Strength is bigger with distance increasing, This means that gluon prohibits quarks and anti-quarks to exist independently. When attempting to pull quarks apart, the quarks cannot escape from the binding of gluons due to reaching the energy required for pair production. (Fig 1.3) This characteristic is referred to as quark confinement.

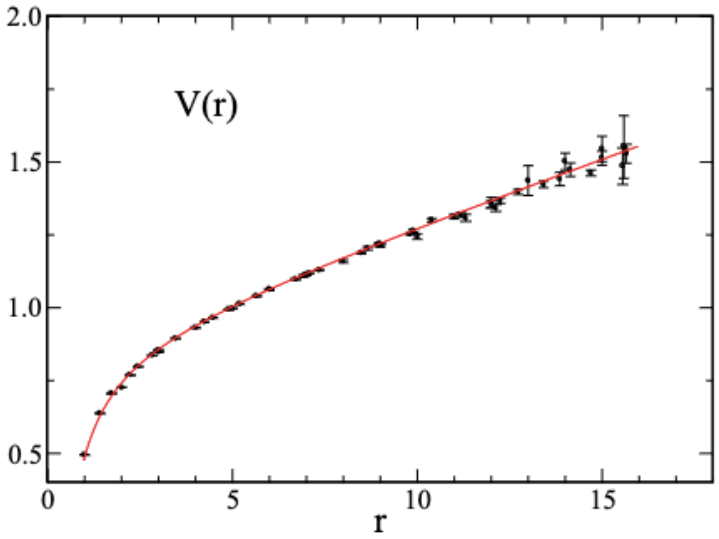

Figure 1.2: Potential between a quark and a anti-quark with lattice QCD calculation[2]

Figure 1.3: Quark confinement

1.2 Quark Gluon Plasma (QGP)

Quark confinement is expected to be broken at high temperatures and densities. In lattice QCD calculations, this occurs due to crossover. This plasma state is called quark-gluon plasma (QCD). The relationship between the QCD phase, temperature, and particle density is shown in Fig 1.4. The QGP has been confirmed to be produced in high-energy nuclear collisions, for example, elliptic flow (v2) and jet-quenching.

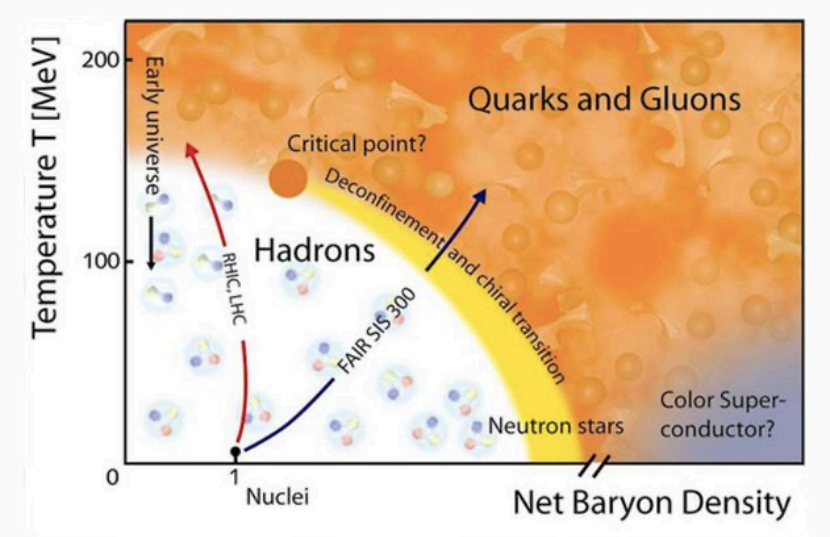

Figure 1.4: QGP phase transition[3]

The anticipated generation of QGP is expected in heavy-ion collisions, such as lead-lead collisions. In nucleon-nucleon or nucleon-heavy-ion collisions, where the parton density in the reaction space is low, the production of QGP is not anticipated.

Elliptic flow refers to geometric features in the phase space of particles. Collective motion resembling an ellipse typically does not occur, but due to the fluid-like behavior of QGP, influenced by the density gradients in the reaction space, a collective expansion takes place. The density gradients arise from geometric features resembling a rugby ball in the reaction region, causing the expansion, or in other words, the phase space to take on an elliptical shape. Indeed, elliptic flow was not observed in proton-proton collisions, but it was observed in lead-lead collisions, thus serving as one of the pieces of evidence for the generation of QGP.

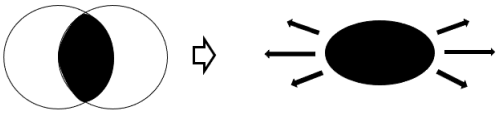

Figure 1.5: Image of flow

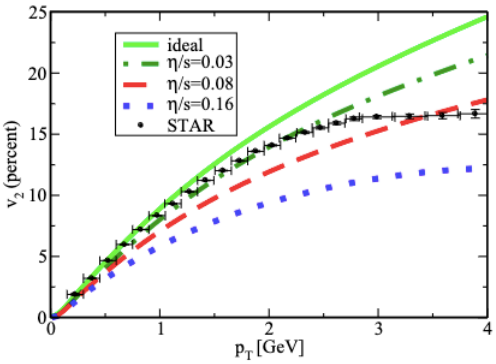

Figure 1.6: Elliptic flow measurement at Star Collaboration [4]

A jet is a narrow, high-transverse-momentum collective motion of particles generated through the fragmentation process of particles associated with hard processes occurring during collisions. The fragmentation process involves particle generation through particle pair production, as illustrated in the previous section's diagram. When two particles associated with a hard process are involved, they are always generated back-to-back. Observations from lead-lead collisions have shown a phenomenon where one of the jets undergoes attenuation. This is interpreted as being caused by energy loss due to gluon radiation in the QGP. This phenomenon serves as one piece of evidence for the generation of QGP in lead-lead collisions.

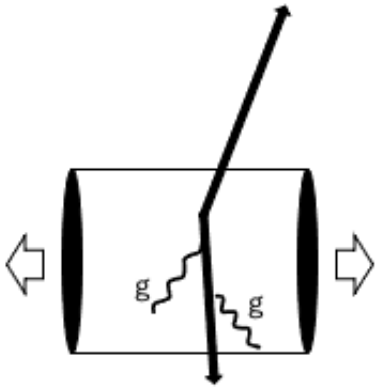

Figure 1.7: jet-quenching image

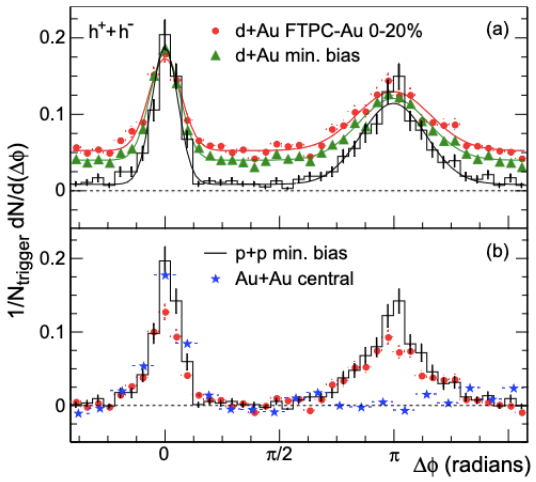

Figure 1.8: Jet quenching measurement at Star Collaboration[5]

1.3 Small system QGP

In the previous section, it was anticipated that Quark-Gluon Plasma (QGP) would not be generated in nucleon-nucleon or nucleon-heavy-ion collisions. However, in recent years, phenomena similar to those observed in heavy-ion collisions have been measured in collisions involving high charged-particle multiplicity. Specifically, phenomena such as elliptic flow, and strangeness hadron enhancement have been observed.

Elliptic flow has been confirmed in high-charged-particle multiplicity p-Pb collisions. The figure illustrates the elliptic flow of J/psi.(FIg 1.8) Similarly, in p-Pb collisions with high-charged-particle multiplicity, an increase in the yield of hadrons containing strange quarks has been observed (Fig 1.9). The data plot for p-Pb approaches Pb-Pb as the multiplicity increases. Thus, high-charged-particle multiplicity p-Pb collisions exhibit behavior similar to Pb-Pb collisions. This challenges the conventional understanding of the mechanisms of particle production and collective motion. To explain these phenomena, various models have been proposed, with examples including Multi-Parton Interaction (MPI) and Color Reconnection (CR).

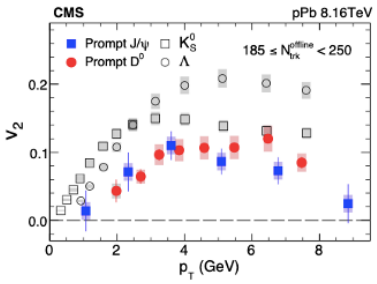

Figure 1.9: Charm meson flow measurement in p-Pb collision[6]

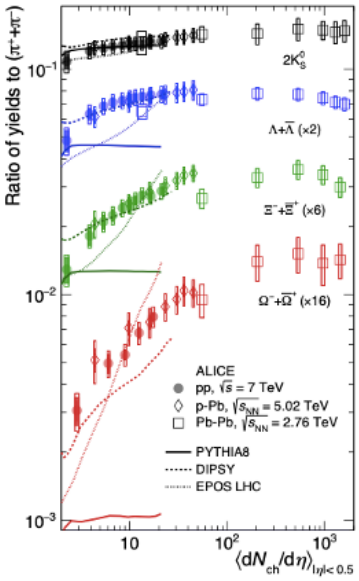

Figure 1.10: Enhanced production of multi-strange hadrons in p-Pb [7]

J/ψ suppression and jet quenching are not observed in p-p and p-Pb collisions. J/ψ suppression is also QGP prove observed in heavy-ion collisions. (See Sec.1.6)

1.4 Multi-parton interaction (MPI)

MPI (Multi-Parton Interaction) is a phenomenon that involves multiple parton scatterings during the collision of nucleons (Fig 1.10). PYTHIA is one

of the models that introduces MPI. In PYTHIA, the consideration of impact parameters is extended to proton-proton collisions, and the probability of MPI occurrence increases with the rising centrality. The charged-particle multiplicity observed in LHC's CDF aligns with the predictions of PYTHIA, which incorporates MPI (Fig 1.11).

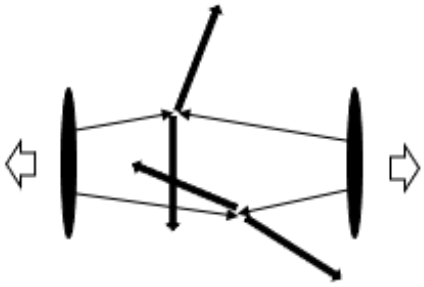

Figure 1.11: Image of MPI at p-p collision

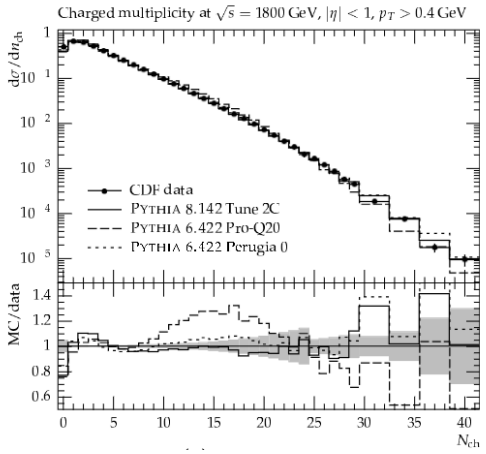

Figure 1.12: Charged-particle multiplicity measurement vs PYTHIA[8]

1.5 Color reconnection (CR)

The color reconnection is introduced to describe collective motion of particles like elliptic flow. When MPI occurs, different parton collisions are initially

considered independent, but as generated particles and colliding partons become connected by strings, they undergo attraction, causing changes in the phase space distribution. CR is a model that captures this behavior.

The Fig 1.12 illustrates the sequence from MPI to CR. In (a), the first parton collision occurs, and in (b), when the second parton collision occurs, the strings associated with the two collision events undergo reconnection, resulting in the configuration shown in (c).

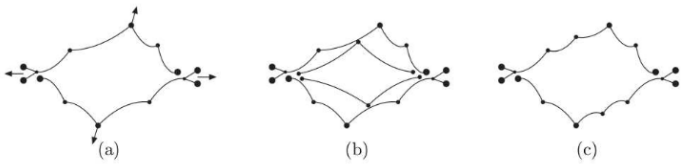

Figure 1.13: Color reconnection process [9]

Without CR, the string configuration is like (a), causing the generated particles to be pulled toward the beam. However, when CR occurs, strings connect particles moving in the direction perpendicular to the beam axis, leading to an increase in transverse momentum compared to the case without CR.

Fig 1.13 shows the dependence of average transverse momentum on charged-particle multiplicity. It compares the results from the PYTHIA event simulator, which incorporates both MPI and CR, with the case where CR is absent. In the absence of CR, the average values are flat since parton collisions in MPI do not interact with each other. With CR, an increasing trend is observed, aligning with experimental results.

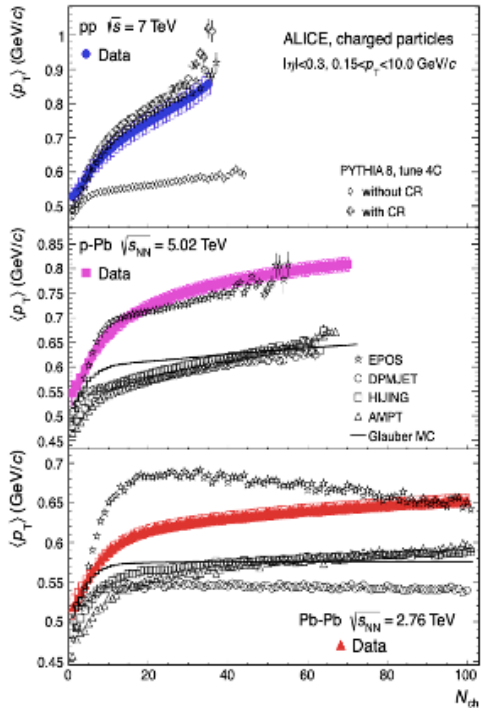

Figure 1.14: Mean transverse momentum measurement vs PYTHIA w/o CR

1.6 J/ψ production suppression in small systems

Charmonium yield as a function of charged-particle multiplicity can reflect both MPI and QGP signature. MPI was originally used to describe particle generation through soft processes, but in high-energy collisions like those at the LHC, there is a possibility of an increase in hard processes as well. A charm quark is produced at first parton interaction, so the number of charm production as a function of charged-particle multiplicity can reflect the number of parton scattering. J/ψ is a charmonium state composed of a charm and anticharm quark. While the charm pair production is described by pQCD (perturbative Quantum Chromodynamics) since it is a hard process, the transition to the bound state involves soft processes that are not well understood. Charm pair production can occur through processes like Drell-Yan, quark-antiquark annihilation via higher-twist mechanisms, and gluon

fusion. The most predominant process is gluon fusion.

Fig 1.15 illustrates the charged-particle multiplicity dependence of J/psi in ALICE pp collisions at center-of-mass energy 13 TeV. With the increased energy of up to 13 TeV, the self-normalized charged-particle multiplicity reaches up to 8. Faster than linear trend is observed in p-p collisions at both forward and central rapidity. Significant rapid increasing than linear is not seen in p-Pb collisions at forward rapidity. PYTHIA tends to underestimate the J/psi yield beyond 4 in multiplicity at both rapidity range. The difference between forward and central can be due to CR. Previous studies have compared various models focusing on J/psi production in addition to PYTHIA. Those models that approve the data take into account for high gluon density or high order J/ψ production process (3-gluon fusion). The details of these models are described in appendix.

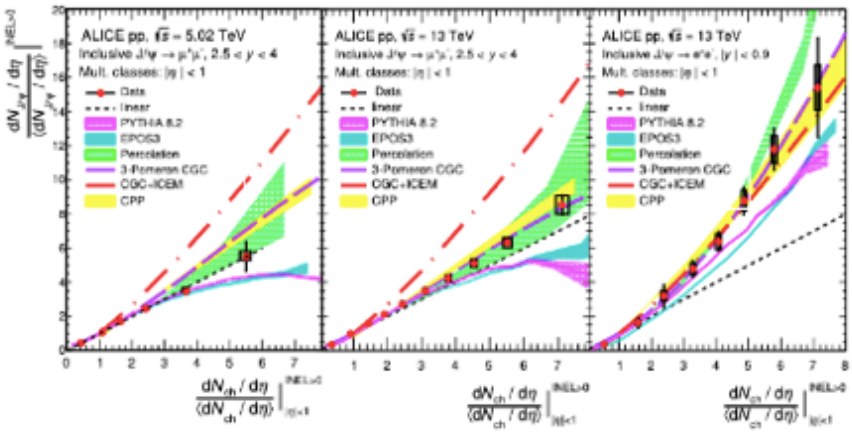

Figure 1.15: J/ψ yield as a function of charged-particle multiplicity with ALICE in central and forward rapidity with model comparison[10]

J/ψ is also one of QGP probe. A bound state formation is prevented by color field of other quarks (color screening) in the QGP. Fig 1.14 shows nuclear modification factor (R_{AA}) with dependence of charged-particle multiplicity in AuAu at center-of-mass energy 200 GeV in PHENIX collaboration. (R_{AA}) means normalized yield by p-p collisions. (R_{AA}) show unit if there is no difference between p-p and AuAu except the number of nucleus-nucleus collisions. The charged-particle multiplicity show how two ions are close

at the moment of collision (centrality). The figure show under unit at all centrality. This proves J/ψ suppression in QGP.

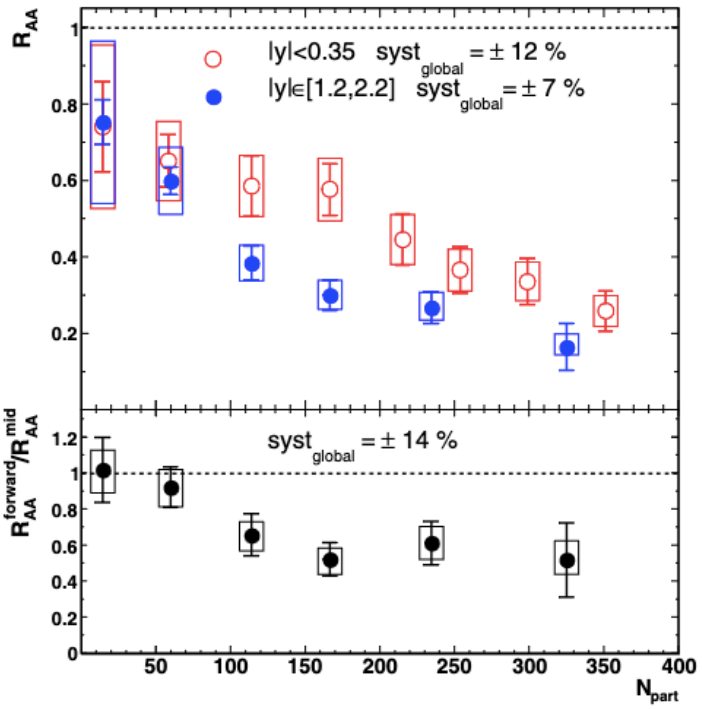

Figure 1.16: $J\psi$ suppression measured by PHENIX in AuAu collisions[11]

As a result, J/ψ is a good prove to understand small systems and QGP.

1.7 Spontaneous breaking of chiral symmetry

The mass of hadrons is significantly larger than the sum of the masses of their constituent quarks. For instance, the sum of the masses of quarks within a proton constitutes only about 1% of the proton's mass. The remaining mass is believed to originate from the spontaneous breaking of chiral symmetry.

Spin exists in both right- and left-handed components. Particles with zero mass, moving at the speed of light, maintain a consistent spin orientation regardless of the reference frame. This reflects chiral symmetry, which

is symmetric under transformations between right- and left-handed components. In fact, the Lagrangian is preserved even if the wave function in equation (QCD) is written in right-handed and left-handed form($\psi \to \psi_L + \psi_R$) and a rotational transformation is applied to swap the right-handed and left-handed forms.

$$\begin{aligned}\mathcal{L}_{QCD} =& \bar{\psi}_{L,a}(i\gamma^\mu\partial_\mu -)\psi_{L,a} + \bar{\psi}_{R,a}(i\gamma^\mu\partial_\mu)\psi_{R,a} \\ &+ g_s\bar{\psi}_{L,a}\gamma^\mu T^A_{ab}\psi_{L,b}G^A_\mu + g_s\bar{\psi}_{R,a}\gamma^\mu T^A_{ab}\psi_{R,b}G^A_\mu \\ &- \frac{1}{4}G^A_{\mu\nu}G^{A\mu\nu}\end{aligned} \tag{1.5}$$

The chiral rotational transformation is

$$\begin{aligned}&\psi_{LorR} \to U(\theta)\psi_{LorR} \\ &where \\ &U(\theta) = e^{i\theta^a_V T^a}e^{i\gamma^5\theta^a_V T^a}\end{aligned} \tag{1.6}$$

The θ^a_V and θ^a_A terms represent vector and axial transformations respectively. However, mass limits the velocity and changes the orientation of the spin from the point of view of the faster system; the QCD Lagrangian also breaks the chiral symmetry due to the presence of the mass term. The mass term is $-m_q\bar{\psi_L}\psi_R - m_q\bar{\psi_R}\psi_L$ and, This term is not invariant under chiral transformation.

Quarks have mass due to the Higgs mechanism, so the chiral symmetry of hadrons is approximately broken.

At low temperatures, quark condensation occurs, where quark pairs pair up. When quark condensation occurs, the potential takes on the shape of the bottom of a wine bottle, as shown in Fig 1.16 (a) to (b).

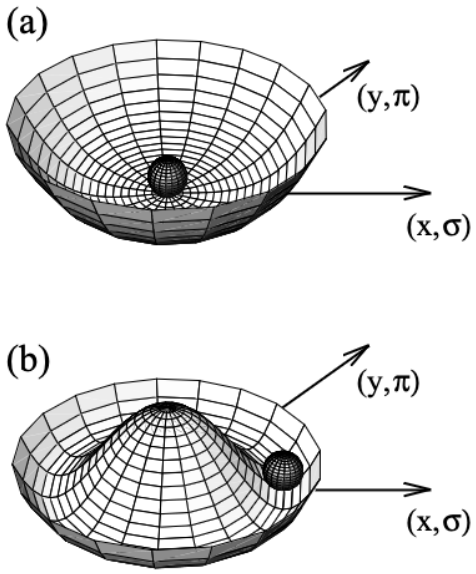

Figure 1.17: Effective potentials[12]

The bottom edge has the same potential at every location, so there is an infinite number of ground states. If a particle takes any one of them at random, it is 'spontaneously' broken.

According to the Nambu-Goldstone theorem, if rotation or chiral symmetry is spontaneously broken, the Nambu-Goldboson is generated. This is a particle of mass zero, of which the π meson is one. In fact, the pi meson has mass, because the u,d quarks acquire mass by the Higgs mechanism.

The mass of the π is derived by the Gelman-Oakes-Lenner relation.

$$f_\pi^2 m_\pi^2 = -(\langle \bar{u}u \rangle + \langle \bar{d}d \rangle)(m_u + m_d) \tag{1.7}$$

The f_π is a constant that represents the strength of the decay process $\pi \to \mu\nu$, and $\langle \bar{q}q \rangle$ is the quark condensation vacuum expectation value for each quark pair. When $m_u = m_d = 0$, the π mass is zero, indicating that it is a type of Southern Goldstone. The hadron mass is larger than the sum of the component masses because it gains mass by the quark condensation vacuum expectation value.

As a result, when quark condensation occurs and spontaneous chiral symmetry breaking occurs, a Nambu Goldboson is produced and gains mass. The Fig 1.17 illustrates the temperature and density dependence of the vacuum expectation value of quark condensation. Similar to the Quark-Gluon Plasma (QGP), this dependence on temperature and density results in a decrease in the expectation value at high temperatures and densities, ultimately reaching zero. This signifies the recovery of chiral symmetry breaking.

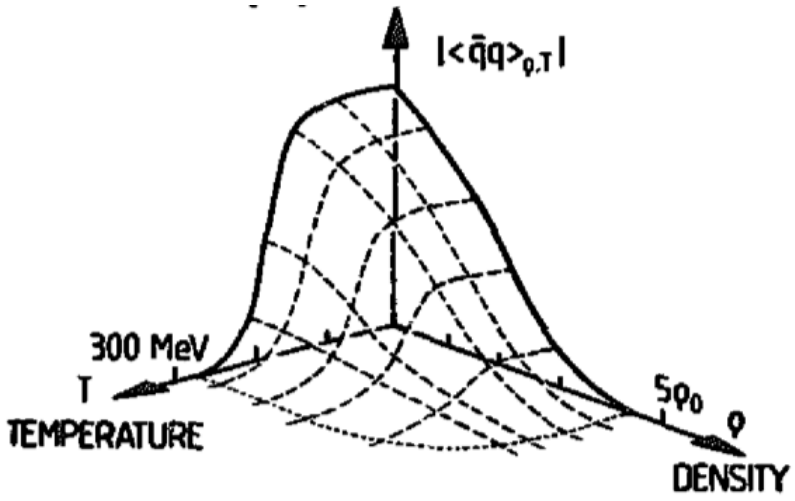

Figure 1.18: Expected value of quark condensation with dependence of temperature and density[13]

1.8 Purpose of this study

This purpose of this study is to observe the generation of QGP in small systems with data taken in 2022 (Run 3)
In Run 3 taken from 2022, the center-of-mass energy of p-p collision improves to 13.6 TeV, whereas 13 TeV in Run 2. The trigger is not imposed (Minimum bias) and statistics are expected to increase by a factor of 10. For forward muon analysis, the spatial resolution is expected to increase by installing the Muon Forward Tracker (MFT) in front of the hadron absorber to remove multiple scattering effects. (See Section 2.4,2.5)

In order to observe QGP in small systems, I measured two physics. the one is J/ψ suppression. The charged-particle multiplicity dependence of J/psi production should show slower increasing than linear with increasing of charged-particle multiplicity.
The other is restoration of spontaneously chiral symmetry breaking. The $\rho + \omega$ mass width should broad in high charged-particle multiplicity.
J/ψ yield as a function of charged-particle multiplicity can reflect small system phenomena like MPI. If QGP is formed in small systems at high charged-particle multiplicity, J/ψ yield suppression should be observed. In proceeding charmonium analysis, There are problems in comparing previous measurement results with models. Specifically, most models (except PYTHIA) calculate only prompt J/psi, while experimental results include contributions from bottomonium (feed-down), which could constitute around 10% of the results. The introduction of new detector is expected to improve position resolution and help eliminate feed-down contributions. In this study, separation between prompt/non-prompt J/ψ is not done.

The measurement of the mass width of the $\rho + \omega$ resonance peak aims to reflect the partial restoration of chiral symmetry, a phenomenon associated with spontaneous symmetry breaking. Low mass vector meson; ρ, ω, and ϕ are well proves of it because of their short lifetime which can makes it possible to decay in the QGP. Furthermore, they decay into dimuon which is not interacted with strong field. Ideally, measuring the mass width of the ρ meson would be preferred. However, due to the close masses of the ρ and ω mesons, making their separation challenging, this study approximates them as a combined $\rho + \omega$ peak. The expectation is that, in a high-temperature state like QGP, where chiral symmetry is expected to be restored, the mass should decrease, thus examining the charged-particle multiplicity dependence of the mass width.

Additionally, this study includes a discussion of the measurement results for the ϕ meson.

Chapter 2

Experimental setup

2.1 LHC

The Large Hadron Collider (LHC) is a particle accelerator ring established by CERN. CERN is located on the border between Swiss and France. LHC consists of two 27km rings and is buried underground. Particles, such as protons and lead ions, are accelerated within a ring, moving in opposite directions in two separate rings. Collision is processed at two beam crossing points.
Run 2 started in 2015 and ended in 2018. Until Run3 which started in 2018, LHC was shut down (LS2). Some upgrade was done during LS2 in LHC and ALICE. Energy increased and reached $\sqrt{s} = 13.6$ TeV in pp and $\sqrt{s} = 5.5$ TeV in Pb-Pb, whereas $\sqrt{s} = 13$ TeV in pp and $\sqrt{s} = 5.02$ TeV in Pb-Pb in Run2. Luminosity was also improved and reach to 13nb^{-1} in PbPb as integrated luminosity, where as 0.4nb^{-1} in Run 2. The beam pipe radius of the crossing point at ALICE is reduced from 29.8 to 19.2 mm.

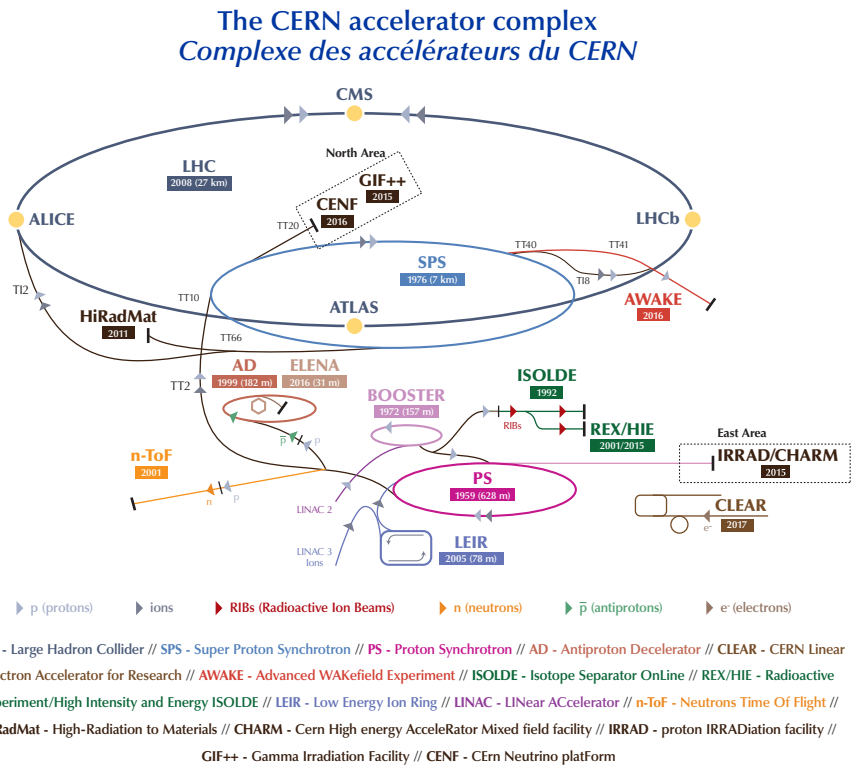

Figure 2.1: CERN LHC[14]

2.2 ALICE setup

A Large Ion Collider Experiment (ALICE) is one of the experiment groups with LHC in CERN. ALICE aims to reveal the QGP signature. ALICE consists of a central rapidity barrel ($|\eta| \leq 0.9$) and forward rapidity muon chamber ($-3.6 \leq \eta \leq -2.5$). The coordinate system in ALICE takes the beam axis as the Z-axis, with positive values extending from the muon chamber towards the central barrel (from right to left in Figure 2.2). The origin point is at the center of the Inner Tracking System (ITS), and collisions are set to occur at it.

Large ALICE upgrades are as follows

- ITS2 install replacing ITS
- Muon Foward Tracker (MFT) install

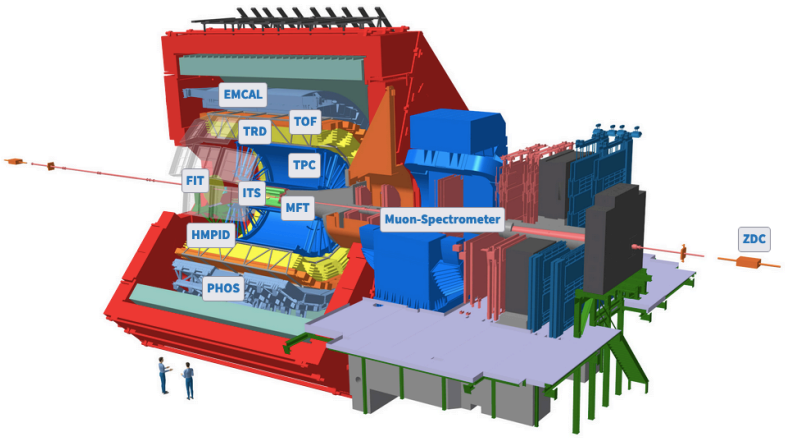

Figure 2.2: ALICE detectors[15]

• Online Ofline (O2) system install
ITS2 has seven planes obtained by silicon pixel sensors. MFT is a new tracking detector located in front of the hadron absorber to improve spatial resolution for the muon detector system. Show detail in section 2.5. O2 system is developed to make it possible to read out events continuously and reconstruct physics parameters online. In Run 2, event triggers, for example, dimuon trigger, and transverse momentum threshold, are required due to poor readout speed. The O2 system is described with details in Sec.2.6.

2.3 Inner Tracking System (ITS2)

ITS2 is the innermost detector covering the beam pipe. The acceptance is $|\eta| \leq 1.22$. ITS plays roles in collision vertex reconstruction, event plane finding, tracking, and measurement of charged-particle multiplicity.
For Run 3, Updated ITS is installed and called ITS2. ITS2 has seven layers whereas ITS has 6 layers. All layers of ITS2 consist of silicon pixel sensors that are excellent in terms of spatial resolution. Silicon pixel sensor is used in ITS inner two layers, but ITS2 has new sensors based on monolithic active silicon sensor (MAPS).

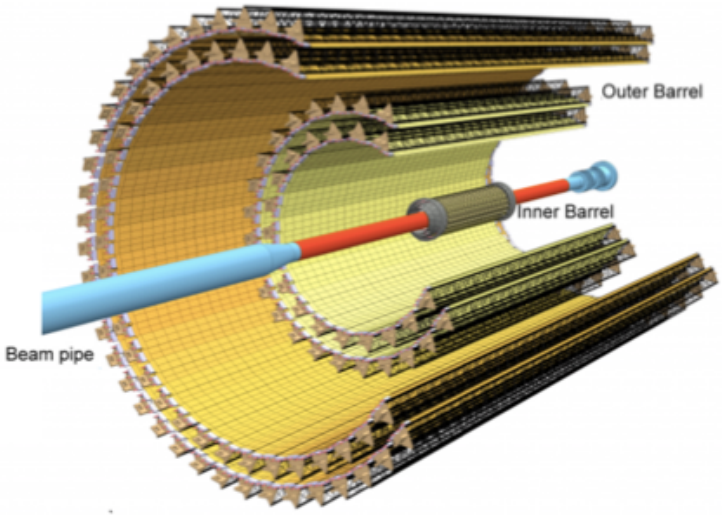

Figure 2.3: ITS2[16]

2.4 Forward muon detector system

The muon spectrometer identifies muons by hadron absorber to absorb and remove particles except muon. Their acceptance is $-4 \leq \eta \leq -2.5$. Beyond the hadron absorber, it consists of the Muon Chamber (MCH), composed of five tracking detectors and a dipole magnet for momentum measurement, the Muon Identifier (MID) consisting of two resistive plate chambers, and the MID-Shield designed to eliminate particles except muon that have passed through the hadron absorber. It's a massive detection system spanning 16.2m from the hadron absorber to the second layer of MID. The characteristics of each component are described below.[20]

• Hadron Absorber: A 4m thick absorber made of carbon, iron, and concrete. It allows muon with a momentum of p 4 to pass through (-5.03m z -0.9m).
• MCH: Consists of five tracking detectors with a position resolution of 100 μ m. Two are placed in front of the dipole magnet, one in the middle, and two at the back.
• Dipole Magnet: Generates a 0.7T magnetic field parallel to the beam axis

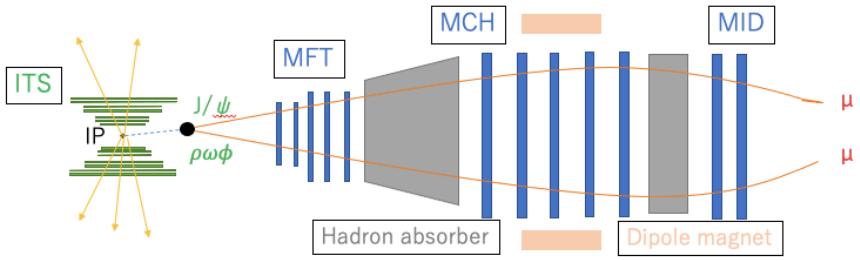

Figure 2.4: Forwad muon detector system in Run 3

(-9.85m z -5m).
• MID-Shield: A 1.2m thick iron absorber designed to absorb hadrons that have passed through the hadron absorber.
• MID: Consists of two resistive plate chambers with a time resolution of 2ns for triggering and identifying muon more precisely than MCH standalone (-17.1m z -16.1m).

Previously, the muon detector system had inaccuracies in vertex reconstruction due to multiple scattering in the hadron absorber, but it is expected to be improved with the introduction of MFT.

2.5 Muon Forward Tracker(MFT)

This is a new tracking detector to be added to the muon detector system, as mentioned earlier. It is introduced to improve the resolution of the vertex position measurement by performing track reconstruction in front of the hadron absorber. It covers the pseudorapidity range $-3.6 \leq \eta \leq -2.5$. It consists of five plates composed of silicon pixel sensors and is installed in the range of -0.768 z -0.460 along the Z-axis. The position resolution is approximately 5 μ m. With the introduction of MFT, the ability to distinguish muon originating from mesons containing charm quarks (e.g., D mesons) and mesons containing beauty quarks (e.g., B mesons) is anticipated.

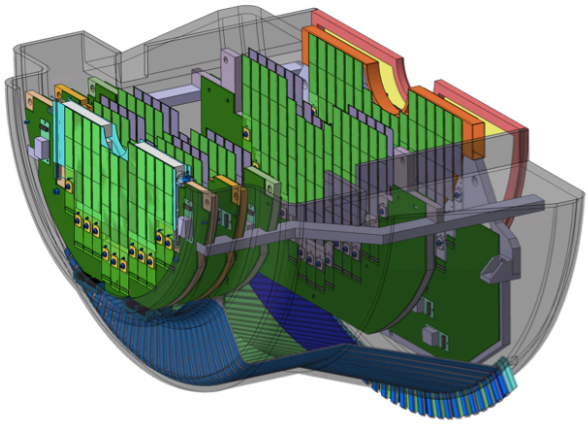

Figure 2.5: MFT[17]

2.6 Online-Offline syetem (O2)

This system is introduced to enable continuous data readout, designed to oversee online data readout, data compression, and offline data analysis. The background of introducing O2 lies in the challenges posed by statistical quantities and data volume in the upgrade. The challenge of statistical quantities arises from the low signal-to-background ratio, while the challenge of data volume comes from the increase in data readout in the Pb-Pb collision experiment in Run 3. The data volume exceeds 1TB/s, roughly 100 times that of Run 1. Therefore, it is necessary to reduce the vast amount of data during readout.
The concept of O2 is to transfer all data sent from detectors to the computing system. It involves dividing time into finely segmented time frames and even finer sub-time frames based on the clock of the LHC. Data from each detector is synchronized within sub-time frames and then within time frames. Calibration and data reconstruction for each detector are performed within sub-time frames and time frames to compress the data, reducing it to 60-70GB/s when sent to the archive. Further asynchronous data reconstruction and parameter calibration for managing data quality are conducted before the final data is stored.

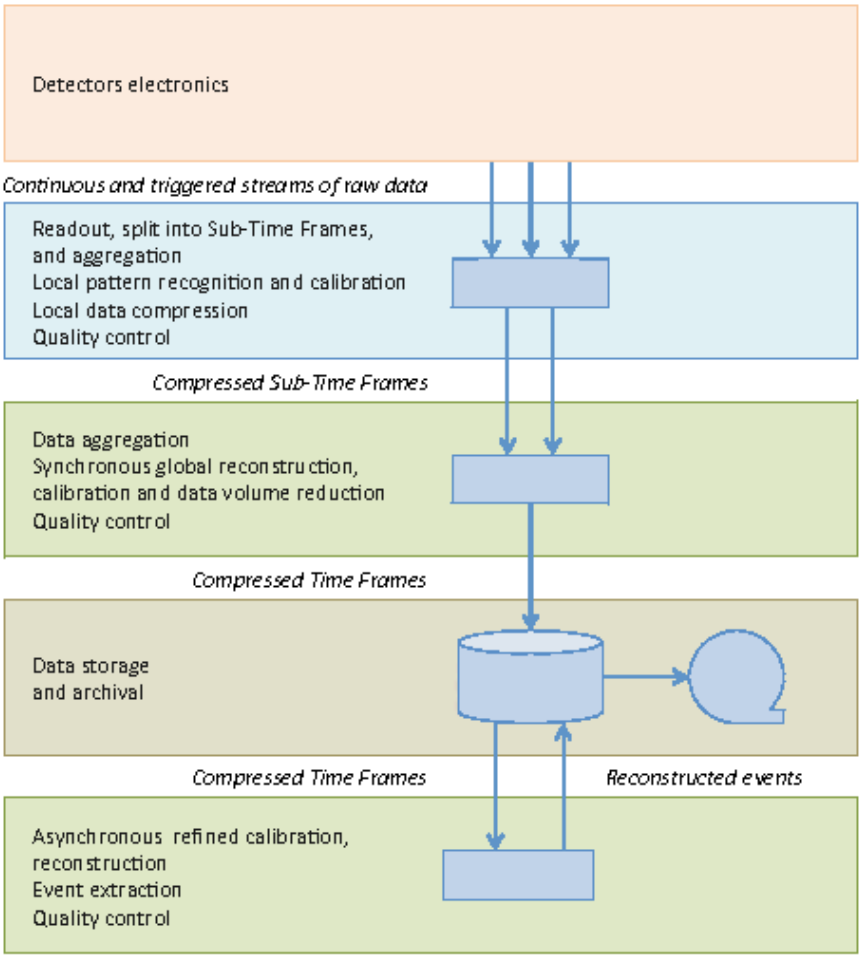

Figure 2.6: Design of O2 system[18]

Chapter 3

Analysis

3.1 Data set

The data set used in this study is Minimum-bias (MB) events with center-of-mass energy $\sqrt{s}$ = 13.6 TeV at pp collision taken in period Run 3. The interaction rate is 500 kHz. The number of reconstructed events is 3.11×10^{11} It should be noted that the data set LHC22o_pass4 that is used in the following discussion has a problem in ϕ angle reconstruction at MCH. Fig 3.1 shows the comparison between LHC22o_pass4 and LHC23_pass1_MCH. LHC23zs_pass1_mch is one of the labels of the dataset taken in 2023 and fixed-version for ϕ angle reconstruction. Asymmetrical distribution is fixed as seen in Fig 3.1 (a). Fig 3.1 (b) illustrates the invariant mass distribution with two datasets. The ϕ angle fixed data show a sharper peak around 3.096GeV/c^2 than the other. However, the number of selected events in ϕ angle fixed data is lower than it of the other by the factor of 40. The LHC23zs_pass1_mch has 7.46×10^9, where as LHC22o_pass4 has 3.11×10^{11}. The statistics affect signal extraction (especially, low mass vector meson) by charged-particle multiplicity separation. Therefore, I selected the LHC22o_pass4 dataset in this study.

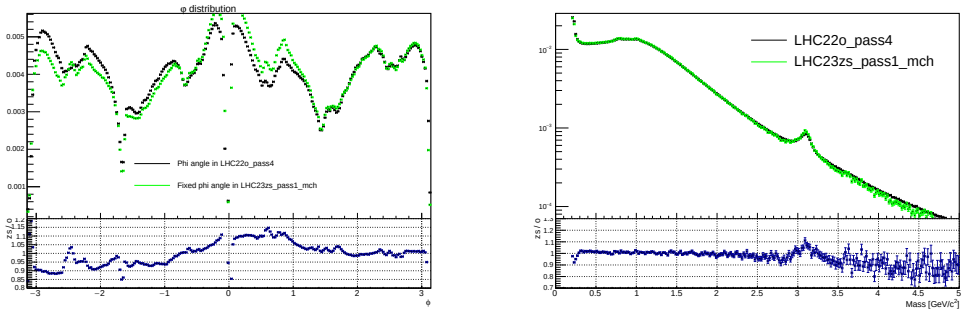

(a) ϕ angle **(b)** Mass

Figure 3.1: ϕ angle and mass comparison between two dataset in top. The ratio of the two distribution (zs / o) is in bottom.

3.2 Event selection

Taken events are MB triggered, but events are selected via some criteria to secure quality. There are two criteria, INEL> 0 and $|z_{col}| \leq 10cm$. INEL ¿ 0 means that there is at least one particle hit in ITS or FIT detector covering beam pipe. z_{col} cut is to ensure the uniformity of the ITS acceptance.

3.3 Charged-particle multiplicity

Charged-particle multiplicity is measured by ITS detector covering pseudo-rapidity range $|\eta| \leq 1.22$. Charged-particle multiplicity($dN_{ch}/d\eta$) should be calculated with the correction number of the reconstructed number of tracks (N_{trk}) to the number of charged-particle (N_{ch}) via detection efficiency with Monte Carlo simulation. In this study, the number of the reconstructed track is not corrected because there is no anchored (corresponding setup to real data taking) MC simulation in the current status. The definition of N_{trk} in this study is the number of ITS tracks that contribute to vertex finding. The criterion is $|DCAy| < 3\sigma_{total}$, where $\sigma_{total} = \sqrt{\sigma^2_{DCAy} + \sigma^2_{vertexX} + \sigma^2_{vertexY} + \sigma^2_{extra}}$. The σ_{extra} is an extra error to mean vertex sigma used when selecting tracks. The σ_{vertex} are given by collision vertex distribution. The σ_{DCAy} is given by the DCAy distribution. Charged-particle multiplicity is normalized by self-expectation value. Fig 3.2 illustrates N_{trk} distribution. The number of events in each multiplicity interval

is referred by it.

$$\frac{(dN_{ch}/d\eta)^i}{\langle dN_{ch}/d\eta\rangle} = \frac{N^i_{trk}}{N_{trk}} \times \frac{N_{MB}}{N^i_{MB}} \tag{3.1}$$

N_{MB} is the number of minimum bias triggered events. The correspondence between $dN_{trk}/d\eta$ and $(dN_{ch}/d\eta)^i/\langle dN_{ch}/d\eta\rangle$ is shown in Table. The N_{trk} interval is adjusted for J/ψ and ρ, ω, ϕ.

Table 3.1: The N_{trk} interval and corresponding charged-particle multiplicity densities

J/ψ		ρ, ω, ϕ	
N_{trk}	$(dN_{ch}/d\eta)^i/\langle dN_{ch}/d\eta\rangle$	N_{trk}	$(dN_{ch}/d\eta)^i/\langle dN_{ch}/d\eta\rangle$
1-10	0.294	1-10	0.294
11-20	0.776	11-20	0.776
21-30	1.30	21-30	1.30
31-40	1.81	31-50	2.00
41-50	2.32	51-100	3.33
51-70	3.02		
71-100	4.24		

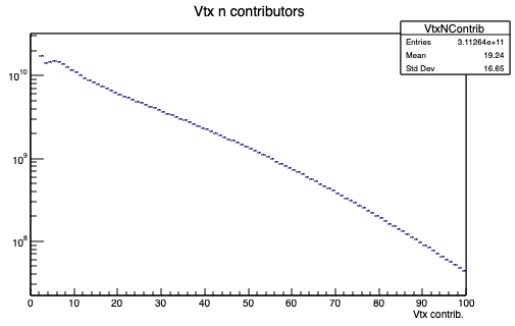

Figure 3.2: Number of ITS tracks contributes to primary vertex finfing

3.4 Invariant mass reconstruction with dimuon

Stored forward tracks contain MCH tracks. All tracks used in this study are matched to both MFT and MID and called Global-Muon-Track (GMT).

MFT-MID matching secure muon identification due to the iron wall located between MCH and MID. MFT-MCH matching improves spatial resolution. Muon track cuts required to GMT are shown in Table.

Table 3.2: Muon track selection

Indicator	criteria
R_{abs}	$17.5 \leq R_{abs} \leq 89.5$
$pDCA$	$pDCA \leq 594(17.5 \leq R_{abs} \leq 26.5)$
	$pDCA \leq 324(26.5 \leq R_{abs} \leq 89.5)$
η	$-4 \leq \eta \leq -2.5$

R_{abs} is the distance from the z-axis at the end of the absorber. That is used to remove tracks that go through the high-density part of the absorber. The tracks are affected by multiple scattering significantly. The $pDCA$ means moment times distance from the closest approach (DCA). DCA is the distance from the z-axis to the point propagated to z_{col}. DCA is multiplied by momentum to cancel its momentum dependence. The larger the lifetime of a particle is, the larger its $pDCA$ tends to be. The $pDCA$ selection removes muon from long lifetime particles, π, K. The η selection reflects MCH acceptance.
Invariant mass reconstruction is for signal particle extraction. Resonance peak in mass distribution indicates signal.

$$M_{\mu\mu} = \sqrt{2m_{\mu}^2 + 2(E_{\mu 1}E_{\mu 2} - p_{\mu 1} \cdot p_{\mu 2})} \tag{3.2}$$

where

$$E_{\mu} = \sqrt{m_{\mu}^2 + p_{\mu}^2} \tag{3.3}$$

Fig 3.3 is the 2D-histogram via the invariant mass reconstructed in forward and N_{trk} measured in central. The following analysis is based on it.

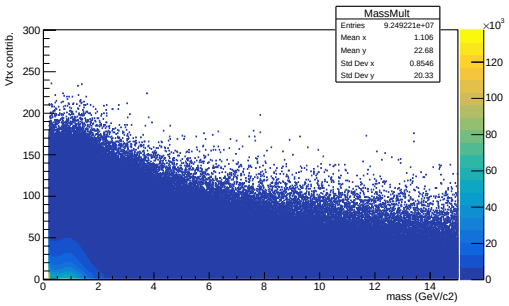

Figure 3.3: Invariant mass vs N_{trk}

3.5 Combinatorial Background(BG) subtraction

Invariant mass distribution is calculated by all opposite sign track pairs in the same event. Pairing can contain no correlation and is called combinatorial BG. There are two well-known methods to subtract combinatorial BG, like-sign method and event mixing method.

3.5.1 Like-sign (LS) method

The like-sign (LS) method uses the invariant mass spectrum via the like-sign pairs (plus-plus or minus-minus pairs). Correlated muon pair production is via dimuon pair production, so the like-sign pairs are considered noncorrelation pairs.

$$\frac{dN_{BG}}{dm} = 2R\sqrt{\frac{dN^{++}_{same}}{dm}\frac{dN^{++}_{same}}{dm}} \tag{3.4}$$

where

$$R = \frac{\frac{dN^{+-}_{mix}}{dm}}{2\sqrt{\frac{dN^{++}_{mix}}{dm}\frac{dN^{++}_{mix}}{dm}}} \tag{3.5}$$

R factor is to correct the difference between plus charge and minus charge acceptance. $\frac{N_{mix}}{dm}$ is obtained by event mixing pairing where as $\frac{N_{same}}{dm}$ is contained by same event pairing. Event mixing pairing means that the counterpart of a pairing originates from different events. The Fig3.3 shows mass

distribution with combinatorial BG estimated by the LS method at the top and Rfactor at the bottom. Interval of N_{trk} dependence of Rfactor is weak. Rfactor shows unit in $m_{\mu\mu}leq0.5$, where as smaller than unit in $m_{\mu\mu}geq0.5$. Rfactor affects low mass region, but not resonance peak of signals.

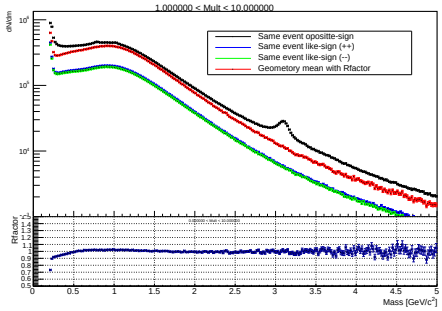

(a) $1 \leq N_{trk} \leq 10$

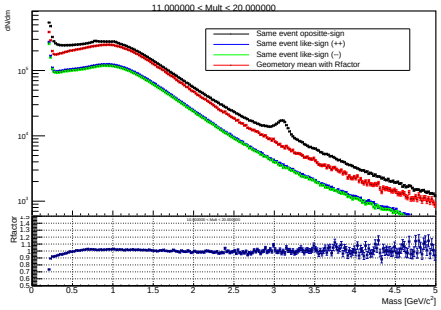

(b) $11 \leq N_{trk} \leq 20$

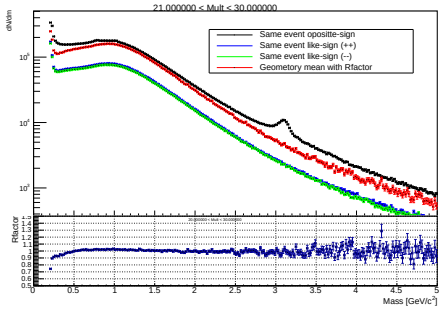

(c) $21 \leq N_{trk} \leq 30$

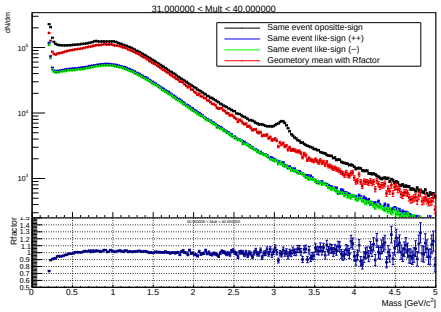

(d) $31 \leq N_{trk} \leq 40$

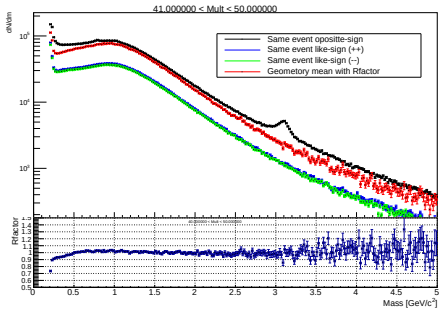

(e) $41 \leq N_{trk} \leq 50$

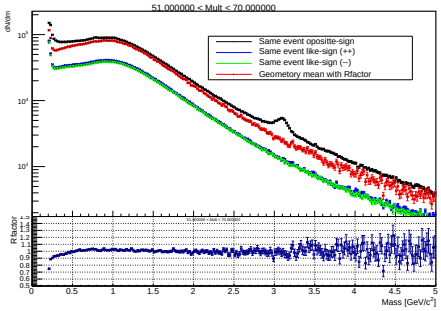

(f) $51 \leq N_{trk} \leq 70$

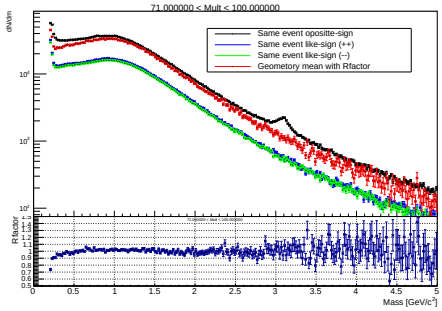

(g) $71 \leq N_{trk} \leq 100$

Figure 3.4: Combinatorial BG with like-sign method and Rfactor

3.5.2 Event mixing (EM) method

The event mixing method forms combinatorial BG via opposite sign track pair, but their origination is not the same. Two events are independent of each other, so pairing in mixed events does not correlate.

$$\frac{dN_{BG}}{dm} = S\frac{dN^{+-}_{mix}}{dm} \tag{3.6}$$

where

$$S = \frac{\int dN^{Like-sign}_{same}}{\int dN^{+-}_{mix}} = \frac{N^{++}_{same} + N^{--}_{same}}{N^{+-}_{mix}} \tag{3.7}$$

S is the scaling factor.
Fig 3.5 illustrates the invariant mass distribution and combinatorial BG estimated by the LS and EM method at the top and the ratio of each at the bottom. The interval of N_{trk} dependence of the LS/EM ratio is weak. Combinatorial BG via the EM method is lower than the LS method in $m_{\mu\mu} \geq 1$, whereas higher than it in $m_{\mu\mu} \leq 1$. the LS method can reflect event-by-event massive motion like flow and jets, whereas the EM method can't. However, the difference in the shape of combinatorial BG via two methods is unclear. All results in this study are done with both combinatorial BG.

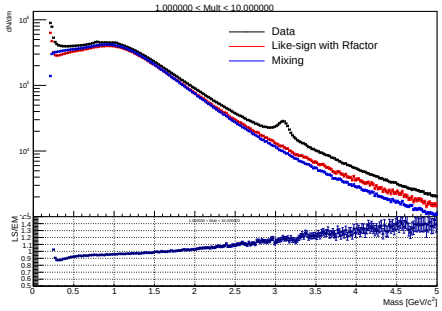

(a) $1 \leq N_{trk} \leq 10$

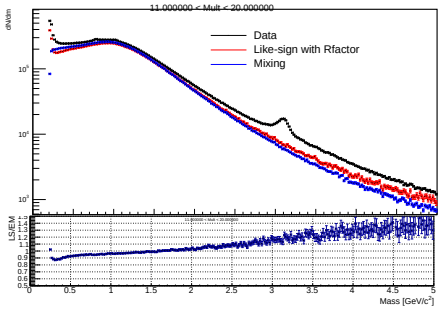

(b) $11 \leq N_{trk} \leq 20$

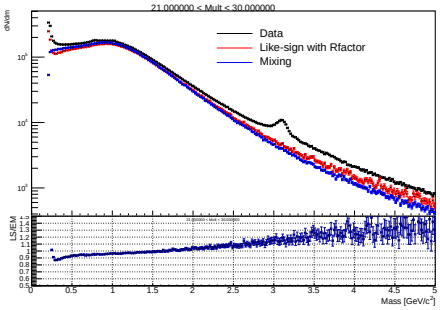

(c) $21 \leq N_{trk} \leq 30$

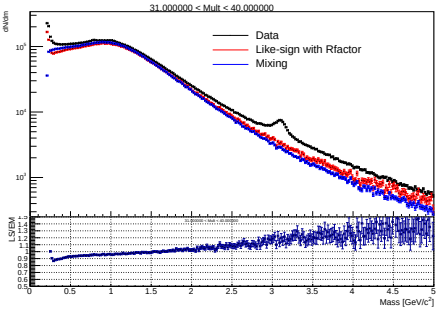

(d) $31 \leq N_{trk} \leq 40$

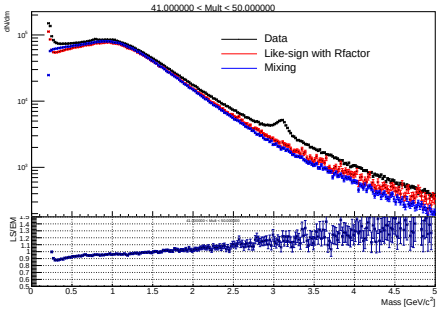

(e) $41 \leq N_{trk} \leq 50$

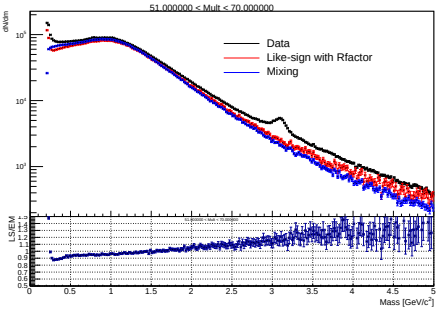

(f) $51 \leq N_{trk} \leq 70$

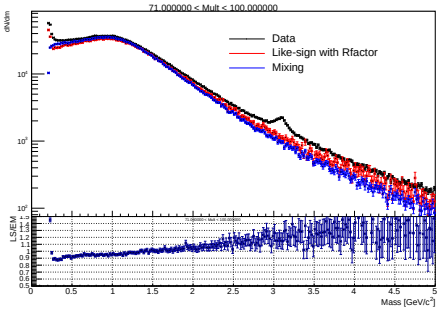

(g) $71 \leq N_{trk} \leq 100$

Figure 3.5: Combinatorial BG with event-mixing method and the ratio LS/EM

3.6 Signal extraction

Resonance peak should follow Breit-Wigner formula.

$$f(x) = \frac{k}{(x^2 - M^2)^2 + M^2\Gamma^2} \tag{3.8}$$

where

$$k = \frac{2sqrt2M\Gamma\gamma}{\pi\sqrt{M^2+\gamma}}, \gamma = \sqrt{M^2(M^2+\Gamma^2)} \tag{3.9}$$

However, the decay width Γ can be broad due to momentum and opening angle resolution and energy loss in detectors and other objects. As a result, a Gaussian-based function is used to extract signals. The double-sided crystal ball function and Gaussian are used for J/ψ and $\rho, \omega, and \phi$ extraction as signal functions. Remaining BG are estimated with double exponential function for high mass ($2 \leq M \leq 4(GeV/c^2)$) region, and Variable Width Gaussian (VWG) function and single exponential function for low mass ($0.5 \leq M \leq 1.35(GeV/c^2)$) region. The double-sided crystal ball function has two tails on both the high-mass side and low-mass side. Tails can reflect detector resolution and energy loss effects. CB2 function is

$$f_{CB2} = \begin{cases} (\frac{\beta_1}{|\alpha_1|})^{\beta_1} e^{-\frac{\alpha_1^2}{2}} (\frac{\beta_1}{|\alpha_1|} - |\alpha_1| - \frac{x-m}{\sigma})^{-\beta_1} & (\frac{x-m}{\sigma} \leq \alpha_1) \\ e^{-\frac{(x-m)^2}{2\sigma^2}} & (\alpha_2 < \frac{x-m}{\sigma} < \alpha_1) \\ (\frac{\beta_2}{|\alpha_2|})^{\beta_2} e^{-\frac{\alpha_2^2}{2}} (\frac{\beta_2}{|\alpha_2|} - |\alpha_2| + \frac{x-m}{\sigma})^{-\beta_2} & (\frac{x-m}{\sigma} \geq \alpha_2) \end{cases} \tag{3.10}$$

and VWG function is

$$f_{VWG} = e^{-\frac{(x-m)^2}{2\sigma(x)^2}} \tag{3.11}$$

where

$$\sigma(x) = A + B(\frac{x-m}{m}) \tag{3.12}$$

The yield at each N_{trk} interval is normalized by its expectation value of multiplicity integrated yield.

$$\frac{(dN_{Sig}/dy)^i}{\langle dN_{Sig}/dy \rangle} = \frac{N^i_{Sig}}{N_{Sig}} \times \frac{N_{MB}}{N^i_{MB}} \tag{3.13}$$

Fig 3.6 3.8 illustrate J/ψ extraction with CB2 function in each multiplicity interval in case w/o LS and EM method to estimate combinatorial BG.

The remaining BG is fit by the double exponential function. The remaining BG is fit well. Fitting χ^2 is shown in the next chapter. The asymmetry behavior of J/ψ resonance peak is illustrated by the tails of CB2 function (red line).

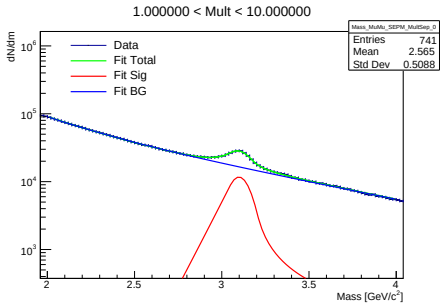

(a) $1 \leq N_{trk} \leq 10$

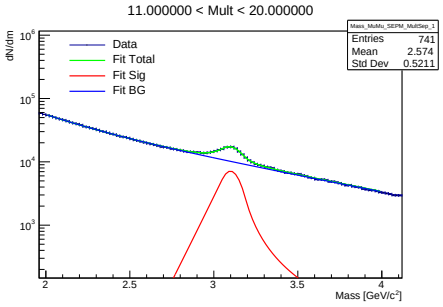

(b) $11 \leq N_{trk} \leq 20$

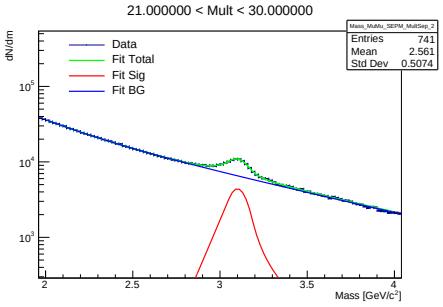

(c) $21 \leq N_{trk} \leq 30$

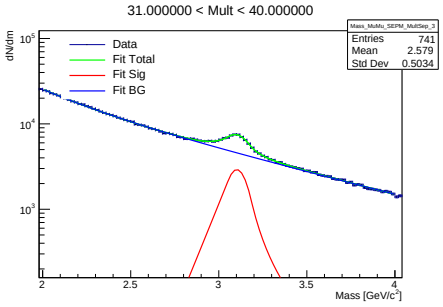

(d) $31 \leq N_{trk} \leq 40$

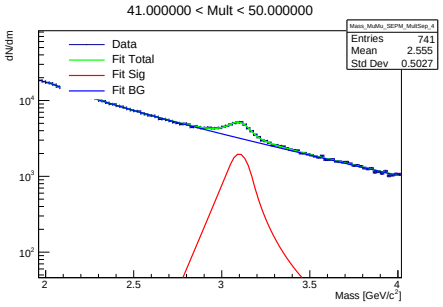

(e) $41 \leq N_{trk} \leq 50$

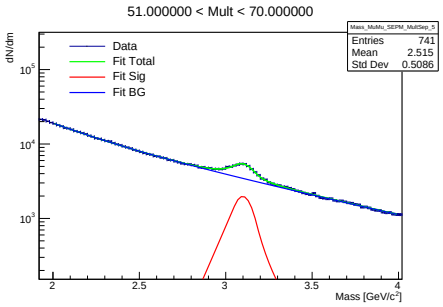

(f) $51 \leq N_{trk} \leq 70$

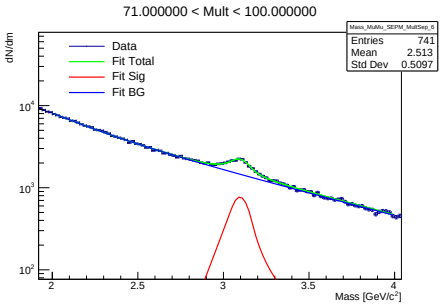

(g) $71 \leq N_{trk} \leq 100$

Figure 3.6: J/ψ signal extraction without combinatorial BG subtraction

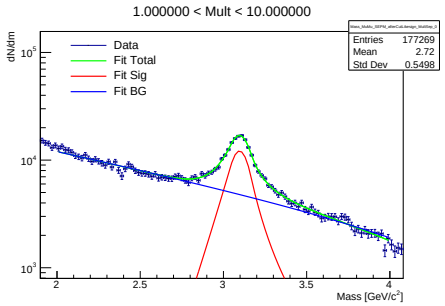

(a) $1 \leq N_{trk} \leq 10$

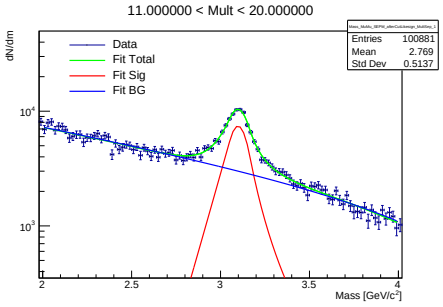

(b) $11 \leq N_{trk} \leq 20$

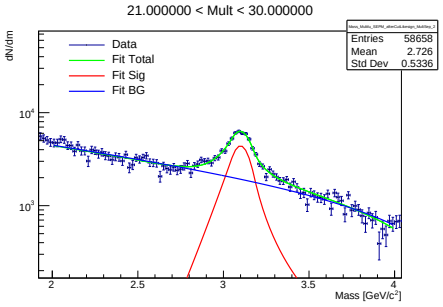

(c) $21 \leq N_{trk} \leq 30$

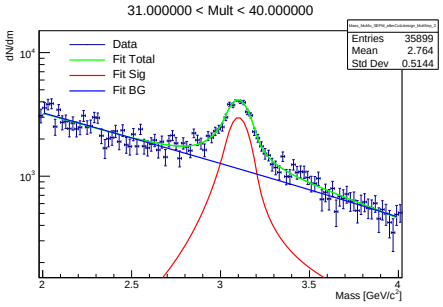

(d) $31 \leq N_{trk} \leq 40$

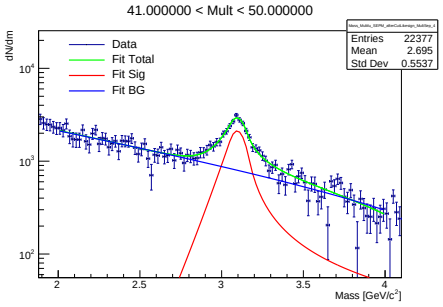

(e) $41 \leq N_{trk} \leq 50$

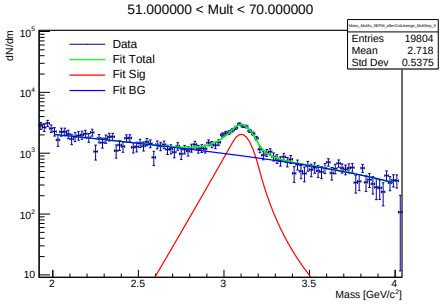

(f) $51 \leq N_{trk} \leq 70$

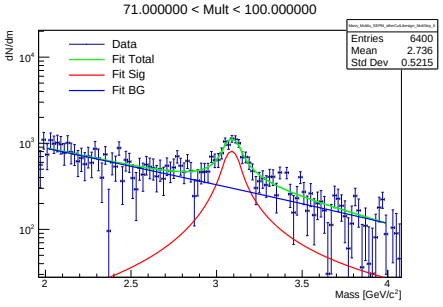

(g) $71 \leq N_{trk} \leq 100$

Figure 3.7: J/ψ signal extraction with LS method

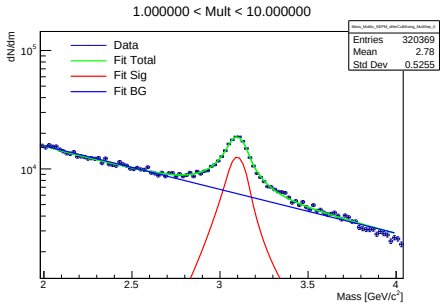

(a) $1 \leq N_{trk} \leq 10$

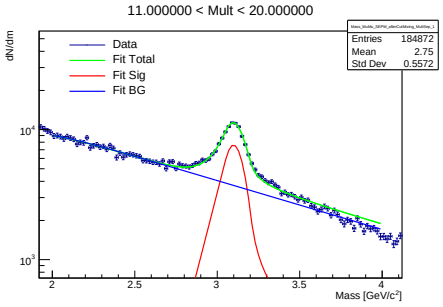

(b) $11 \leq N_{trk} \leq 20$

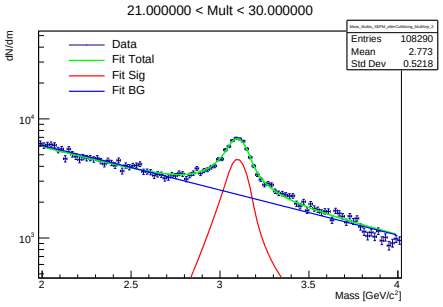

(c) $21 \leq N_{trk} \leq 30$

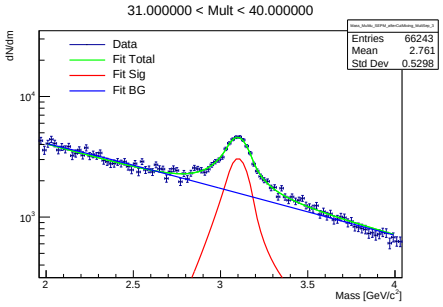

(d) $31 \leq N_{trk} \leq 40$

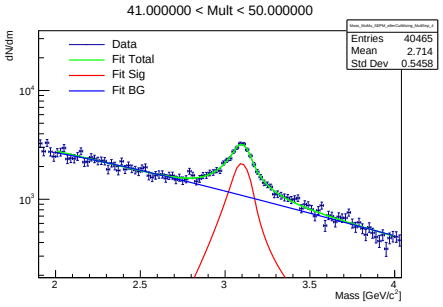

(e) $41 \leq N_{trk} \leq 50$

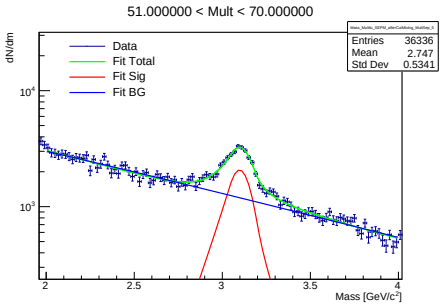

(f) $51 \leq N_{trk} \leq 70$

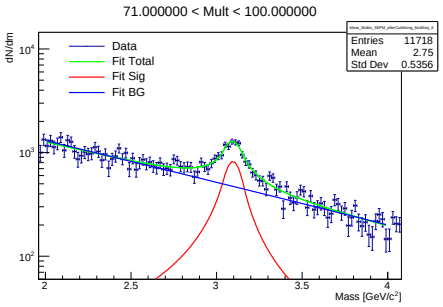

(g) $71 \leq N_{trk} \leq 100$

Figure 3.8: J/ψ signal extraction with EM method

Fig 3.9 3.12 show $\rho+\omega$ and ϕ extraction in each multiplicity range in case of using the LS and EM method to estimate combinatorial BG. Different from J/ψ extraction, low mass meson resonance peak is so significantly affected by combinatorial BG (see Fig 3.3) that extraction is done after combinatorial BG subtraction. The size of the signals strongly depends on the estimation of the remaining BG after combinatorial subtraction. Two remaining BG functions are used, the VWG function and the single exponential function. Fig 3.9 and 3.10 are results with exponential function and Fig 3.11 and 3.12 are with VWG function. See Fig 3.10 (d), the remaining BG function (exponential) overestimates between $\rho+\omega$ and ϕ peaks. In the highest multiplicity interval ($51 \leq N_{trk} \leq 100$), signal resonance peaks are not clear to fit, especially ϕ with the LS method.

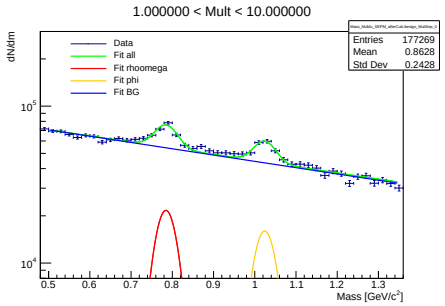

(a) $1 \leq N_{trk} \leq 10$

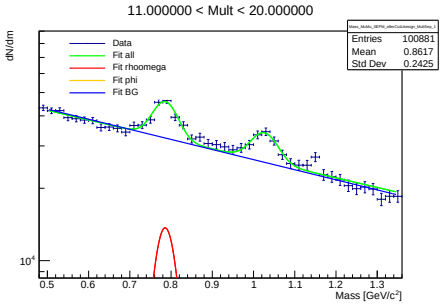

(b) $11 \leq N_{trk} \leq 20$

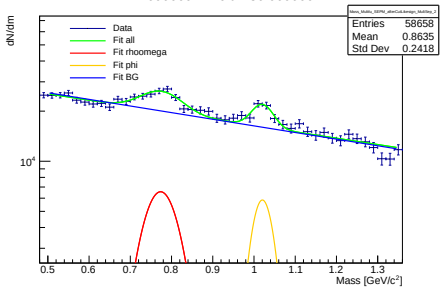

(c) $21 \leq N_{trk} \leq 30$

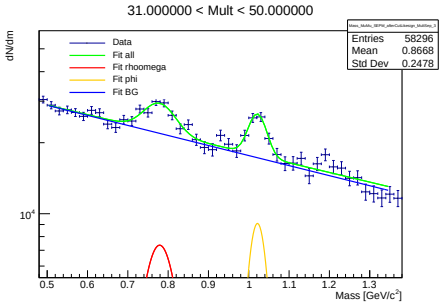

(d) $31 \leq N_{trk} \leq 40$

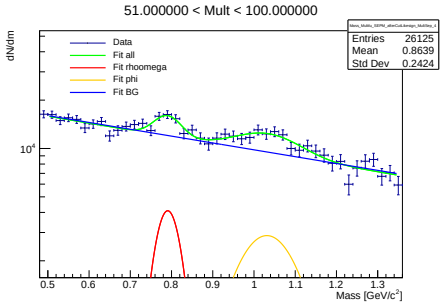

(e) $41 \leq N_{trk} \leq 50$

Figure 3.9: ρ+ω and ϕ extraction (combinatorial BG is estimated by LS method, remaining BG is done by exponential function)

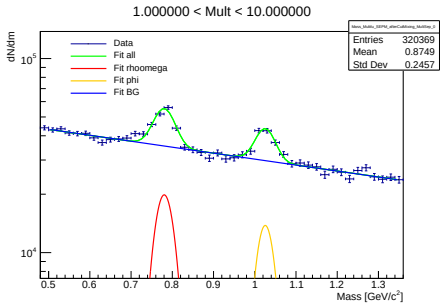

(a) $1 \leq N_{trk} \leq 10$

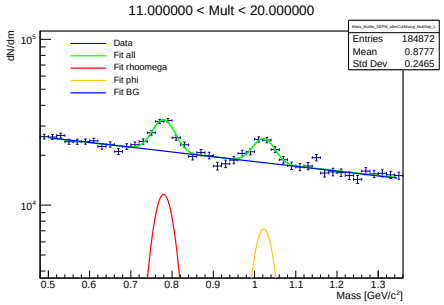

(b) $11 \leq N_{trk} \leq 20$

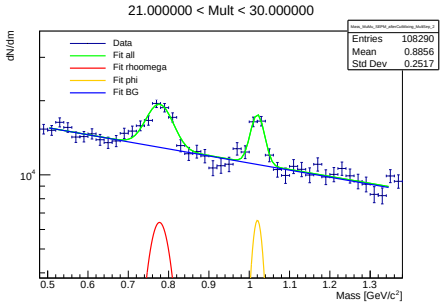

(c) $21 \leq N_{trk} \leq 30$

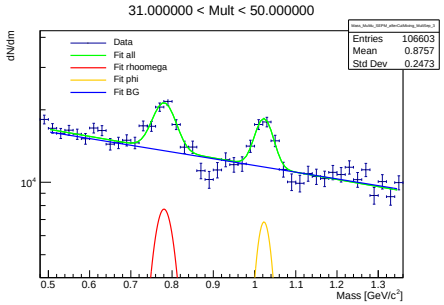

(d) $31 \leq N_{trk} \leq 50$

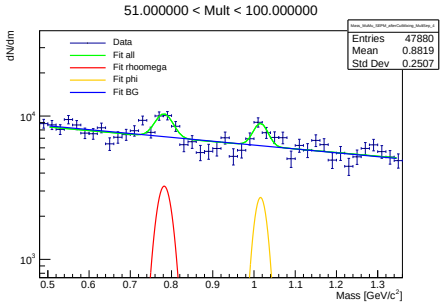

(e) $51 \leq N_{trk} \leq 100$

Figure 3.10: ρ+ω and ϕ extraction (Combinatorial BG is estimated by EM method, remaining BG is done by exponential function)

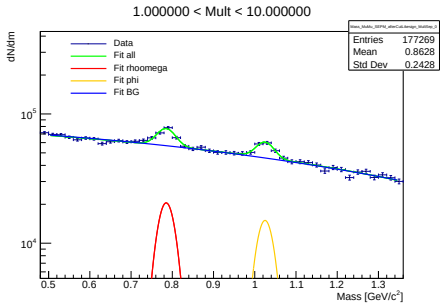

(a) $1 \leq N_{trk} \leq 10$

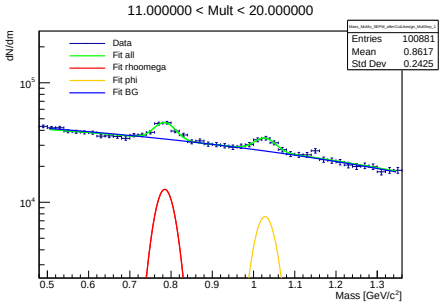

(b) $11 \leq N_{trk} \leq 20$

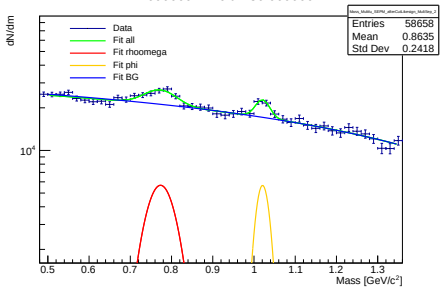

(c) $21 \leq N_{trk} \leq 30$

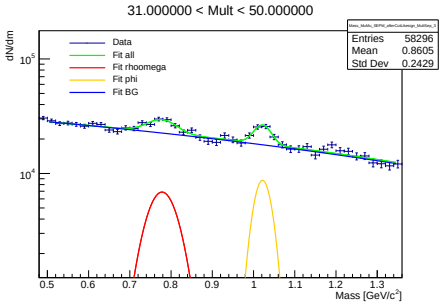

(d) $31 \leq N_{trk} \leq 40$

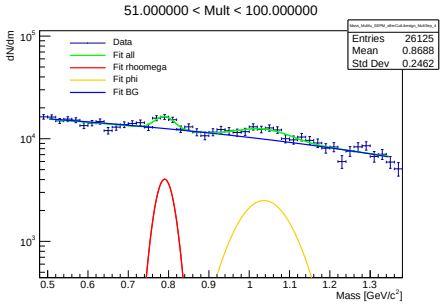

(e) $41 \leq N_{trk} \leq 50$

Figure 3.11: ρ+ω and ϕ extraction (combinatorial BG is estimated by LS method, remaining BG is done by VWG function)

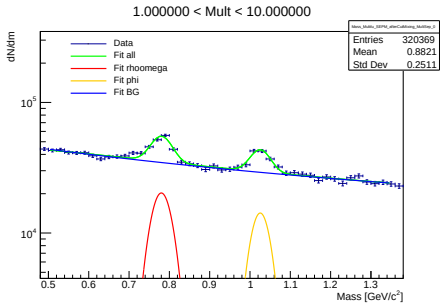

(a) $1 \leq N_{trk} \leq 10$

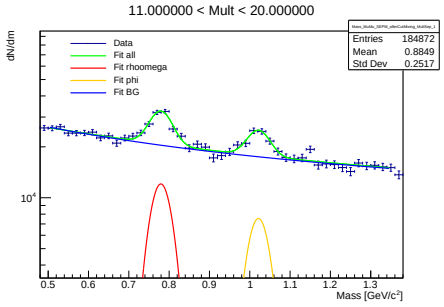

(b) $11 \leq N_{trk} \leq 20$

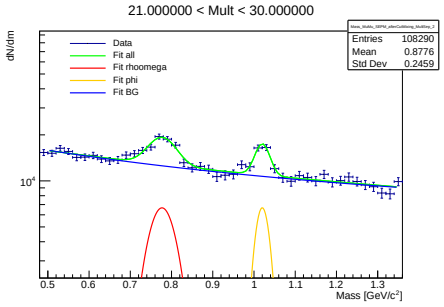

(c) $21 \leq N_{trk} \leq 30$

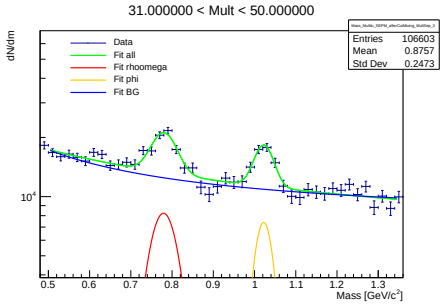

(d) $31 \leq N_{trk} \leq 50$

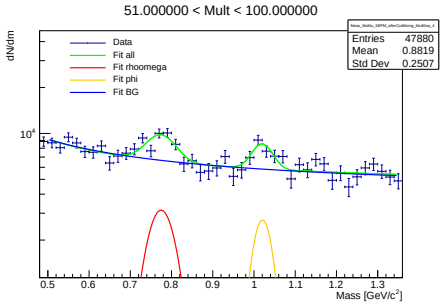

(e) $51 \leq N_{trk} \leq 100$

Figure 3.12: ρ+ω and ϕ extraction (combinatorial BG is estimated by EM method, remaining BG is done by VWG function)

Chapter 4

Result

4.1 J/ψ analysis

Fig 4.1 shows fitting χ^2 of BG + signal total function. The three plots in low charged-particle multiplicity interval (i = 0,1,2) with the LS method are lower than the other two, whereas higher multiplicity plots show similar values. As a result, the case with the LS method shows the most stable fitting.

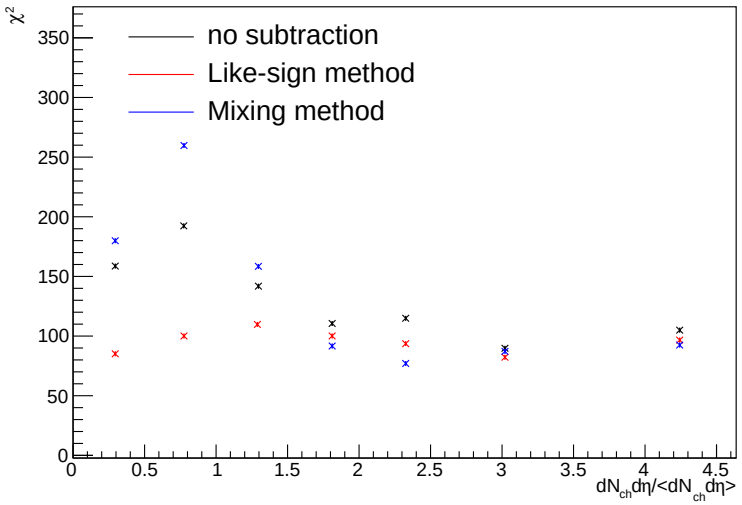

Figure 4.1: Fitting χ^2 with function BG + Signal for J/ψ extraction with dependence of charged-particle multiplicity

Fig 4.2 shows the row yield of J/ψ as a function of charged-particle multiplicity. The appearance of the distribution of each plot does not depend on the method or presence of combinatorial BG estimation, but the size varies and always maintains the relationship EM¿LS¿no-subtraction of combinatorial BG. Table 4.1 summarizes each value and statistics error shown in Fig 4.2. In summary, the yield with the EM method and LS method is higher than it with no subtraction case by 13% (32σ of statistics error) for the EM method and by 6.2%(16σ of statistics error) for the LS method. For resonance peak analysis, peak extraction has a weak dependence on the combinatorial BG estimation method since the remaining BG is removed after combinatorial subtraction. However, statistics errors affect the method, and fitting can be influenced it. I expect that this rho yield difference is due to the fitting process.

[H]

Table 4.1: Fitting χ^2 for lowmass analysis

i	no subtraction	error	LS	error	EM	error
0	110521	683	117600	468	123303	506
1	64291	520	66090	456	71539	382
2	39371	414	41129	282	45364	304
3	26809	346	29817	230	30853	251
4	17576	287	19831	190	20400	206
5	8802	148	9318	96	9995	105
6	2226	62	2497	38	2562	43
Summary	269632	1066	286282	725	304016	782

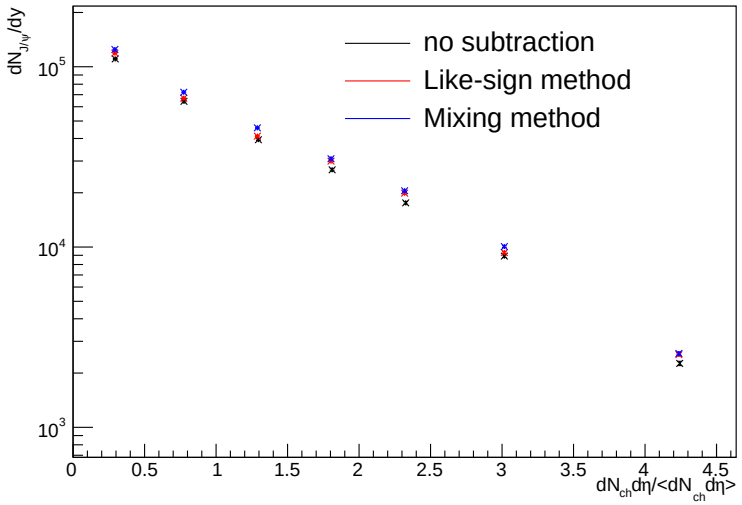

Figure 4.2: J/ψ row yield as a function of charged-particle multiplicity

Fig 4.3 shows the self-normalized yield of J/ψ as a function of charged-particle multiplicity. The self-normalizing process makes the dependence of the combinatorial BG estimation method weak. The three behaviors of normalized yield distribution are similar. Self-normalized yield is increasing gradually from the third charged-particle interval. Statistics error indicates that these enhancement are beyond the margin of error, but the physical meaning of these arguments is unclear, as no correction or systematic error has yet been discussed.

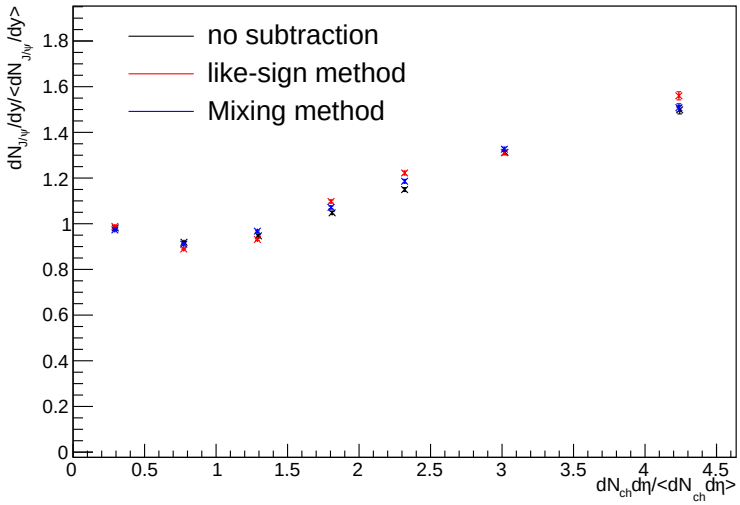

Figure 4.3: Self-normalized J/ψ yield as a function of charged-particle multiplicity[19]

As seen in Fig 1.16, Linear increase at low charged-particle multiplicity has been shown. Increasing may mean that J/ψ production has dependence of multiple parton interaction. Charged-particle multiplicity indicates number of parton-interaction. As a results, Fig 4.3 can imply same behavior as MPI prove. However, Fig 4.3 at low charged-paricle multiplicity doesn't show linear trend.

In order to reveal the cause of yield at low charged-particle multiplicity, I compare with proceeding study.[19] The left one shows the ratio of the number of events at each charged-particle multiplicity intervals. The gaps of values enhance with increasing of charged-particle multiplicity. These imply that results in this study should show more rapid increasing trend. However, there is no evidence to show the cause of strange behavior at low multiplicity range. The right one illustrates the ratio of J/ψ yields with dependence of charged-particle multiplicity. In contrary to the left one, the gaps of the values are shown at the lowest charged-particle multiplicity interval. This gap can cause the enhancement of self-normalized yield at low charged-particle multiplicity range. The strange enhancement of J/ψ yield is not via signal extraction process. This means that accuracy of charged-particle multiplicity

measurement should be investigated more. Ratio of the number of events should be also affected by accuracy of charged-particle multiplicity. Fig 4.3 (a) imply that it may be account for it because this study at the lowest interval show higher value than proceeding study.

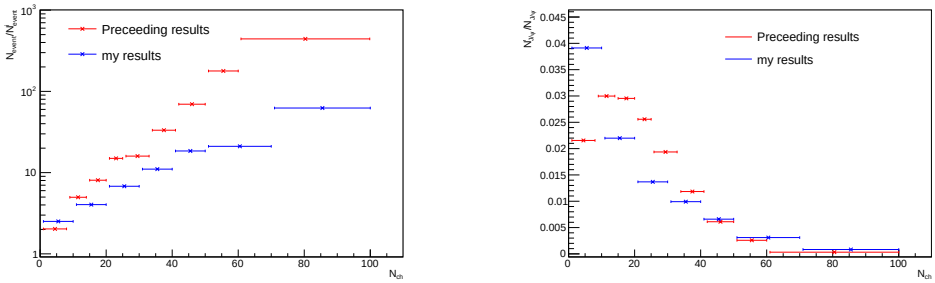

(a) Ratio $N_{event}^{MB}/N_{event}^{MB,i}$ **(b)** Ratio $N_{J/\psi}^{i}/N_{J/\psi}$

Figure 4.4: Ratio $N_{event}^{MB}/N_{event}^{MB,i}$ and Ratio $N_{J/\psi}^{i}/N_{J/\psi}$ with dependence of charged-particle multiplicity

Fig 4.4 illustrates mean mass of J/ψ as a function of charged-particle multiplicity. Mean mass of J/ψ is $\bar{m}_{J/\psi} = 3096.900 \pm 0.006 [\mathrm{MeV/c^2}]$ in PDG. The reconstructed mean mass of J/ψ shows weak dependence of charged-particle multiplicity and PDG value within uncertainties. However, details of the charged-particle multiplicity dependence are not unclear because of its error.

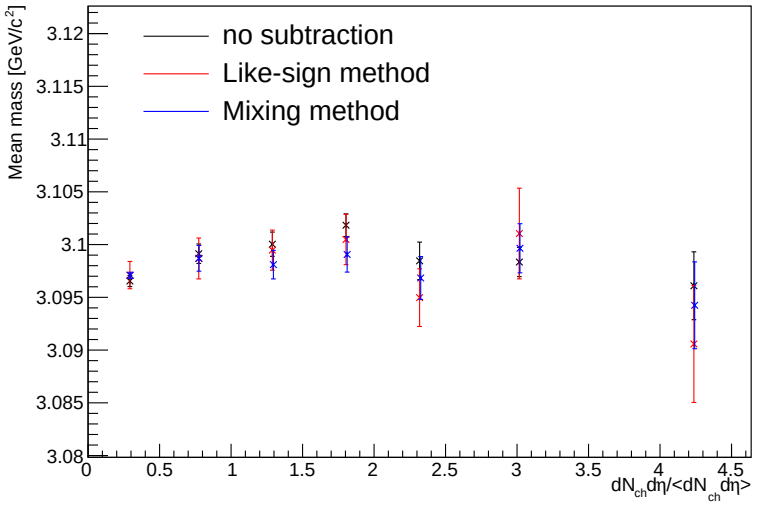

Figure 4.5: J/ψ mean mass as a function of charged-particle multiplicity

Fig 4.5 shows the mass width of J/ψ as a function of charged-particle multiplicity. Decay width of J/ψ is $\Gamma_{J/\psi} = 94.1 \pm 2.7$[keV] with dimuon decay mode in PDG. However, the reconstructed width of J/ψ is higher than PDG one by a factor of 1000 due to detector resolution and energy loss effect. This implies that mass width measurement of J/ψ is difficult to see due to the measurement resolution of the detector.

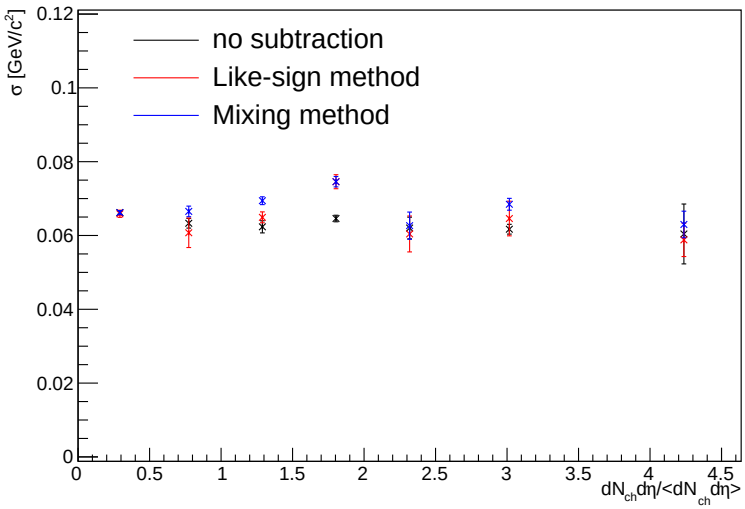

Figure 4.6: J/ψ mass width as a function of charged-particle multiplicity

4.2 Low mass vector meson analysis

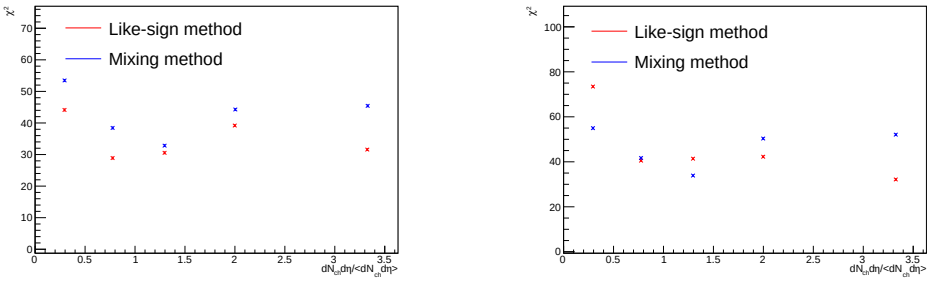

(a) BG : VWG **(b)** BG : Exponential

Figure 4.7: Fitting χ^2 with function BG + Signal for $\rho + \omega and \phi$ extraction with dependence of charged-particle multiplicity

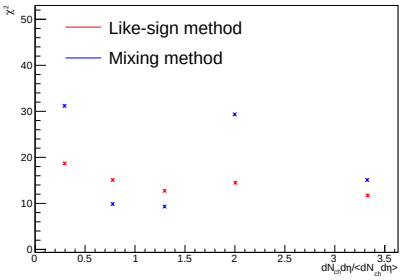

(a) $\rho + \omega$ fitting (BG : VWG)

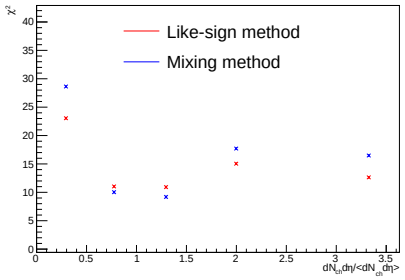

(b) $\rho + \omega$ fitting (BG : Exponential)

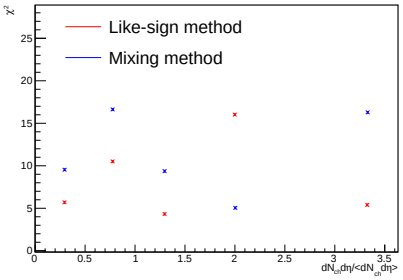

(c) ϕ fitting (BG : VWG)

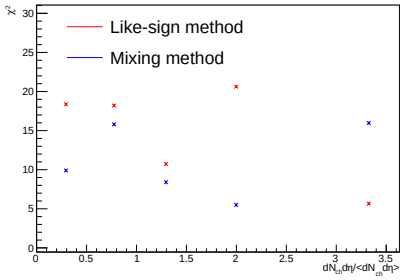

(d) ϕ fitting (BG : Exponential)

Figure 4.8: Signal fitting χ^2 for $\rho + \omega and \phi$ extraction with dependence of charged-particle multiplicity

Fig 4.6 and 4.7 show fitting χ^2 in the case of BG + signal total and signal only with VWG and exponential function. Two distributions of χ^2 fit by VWG and exponential are similar, but averages of χ^2 are a bit different. Table 4.2 summarizes averages of χ^2. Two distributions of χ^2 by using the LS method and EM method are also similar. The difference between the two is not larger than of remaining BG dependence, but the case with the LS method is larger than it with the EM method. Following fitting χ^2 and Fig 3.10 (d) discussed in Sec (3.6), The results with VWG function are discussed in this study. The results with exponential are shown in the appendix.

Fig 4.9 shows the row yield of $\rho + \omega$ and ϕ as a function of charged-particle multiplicity. The dependence of the combinatorial BG estimation method is not small. Table 4.3 summarizes each value and statistics error shown in Fig 4.9. The row yield with the EM method is higher than it with the LS method except for ϕ yield at intervals i = 3 and 4. At the highest charged-particle multiplicity interval, the row yield of ϕ with the LS method is higher than it with the EM method significantly contrary to other plots.

Table 4.2: Fitting χ^2 for lowmass analysis

	LS	EM
VWG		
BG + signal total	34.8	42.9
ρ+ω	14.5	18.9
ϕ	8.3	11.4
Exponential		
BG + signal total	45.8	46.5
ρ+ω	14.5	16.4
ϕ	14.7	11.1

This can be attributed to the ϕ peak being buried in the remaining BG, as can be seen in Fig 3.11 (e). In summary, the yield with the EM method is higher than it with the LS method by 16% (20σ of statistics error) for $\rho + \omega$ and by 7.6%(9.5σ of statistics error) for ϕ. For resonance peak analysis, peak extraction has a weak dependence on the combinatorial BG estimation method since the remaining BG is removed after combinatorial subtraction. However, statistics errors affect the method, and fitting can be influenced it. I expect that this rho yield difference is due to the fitting process.

[H]

Table 4.3: Fitting χ^2 for lowmass analysis

i	LS	error	EM	error
ρ+ω : 0	55449	715	67154	587
1	38856	557	42752	498
2	25309	548	28640	410
3	15798	275	18488	201
4	2189	63	2682	59
Summary	137601	1096	159716	735
ϕ : 0	40086	497	43807	528
1 :	24352	429	27060	429
2 :	11752	282	15093	282
3 :	11584	157	11098	166
4 :	3968	71	1653	47
Summary	91742	735	98710	756

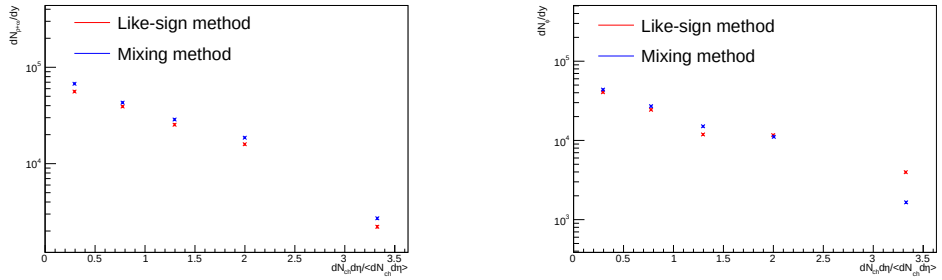

(a) $\rho + \omega$ **(b)** ϕ

Figure 4.9: Row yield as a function of charged-particle multiplicity (BG : VWG)

Fig 4.10 shows the self-normalized yield of $\rho + \omega$ and ϕ as a function of charged-particle multiplicity. The self-normalizing process makes dependence on the combinatorial BG estimation method weak for $\rho + \omega$. However, the two behaviors of normalized yield distribution of $\rho + \omega$ and ϕ are same of the normalized yield distribution of J/ψs. I expect the cause is same, accuracy of charged-particle multiplicity measurement.

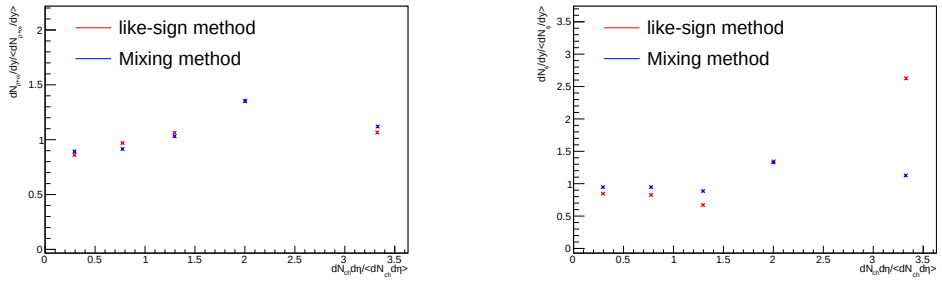

(a) $\rho + \omega$ **(b)** ϕ

Figure 4.10: Self-normalized yield as a function of charged-particle multiplicity (BG : VWG)

Fig 4.11 illustrate the mean mass of $\rho + \omega$ and ϕ as a function of charged-particle multiplicity. Mean mass of low mass vector mesons are $\bar{m}_\rho = 775.26 \pm 0.23[\mathrm{MeV/c^2}]$, $\bar{m}_\omega = 782.66 \pm 0.13[\mathrm{MeV/c^2}]$ and $\bar{m}_\omega = 1019.461 \pm 0.016[\mathrm{MeV/c^2}]$ in PDG. The charged particle multiplicity dependence of mean mass is unclear because of their error, but the mean mass of $\rho + \omega$

shows it of both ρ and ω within uncertainties, and plots of ϕ are within PDG value of ϕ within uncertainties.

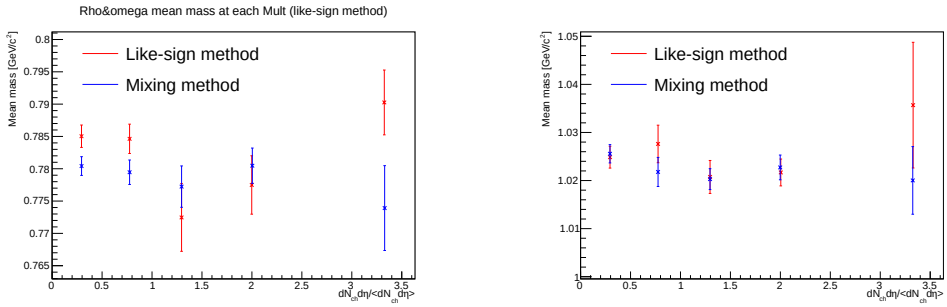

(a) $\rho + \omega$ **(b)** ϕ

Figure 4.11: Mean mass as a function of charged-particle multiplicity (BG : VWG)

The Fig 4.12 show mass width of $\rho + \omega$ and ϕ as a function of charged-particle multiplicity. Decay width of low mass vector mesons are 142.1 ± 8.9[MeV] for ρ, 8.70 ± 0.39[MeV] for ω, and 4.065 ± 0.275[MeV] for ϕin PDG with dielectron channel. However, reconstructed width of $\rho + \omega$ and ϕ is higher than PDG values by a factor of 2 for $\rho + \omega$ compared with PDG of ω and 4 for PDG of ϕ due to detector resolution. The ρ mass width in PDG is so high that can be seen if $\rho + \omega$ is separated independently. In case quality of track reconstruction improves more, the mass width of ω and ϕ can be also observed. In this study, MFT-MCH matching chi2. which reflect how matching is well done is not used for track selection.

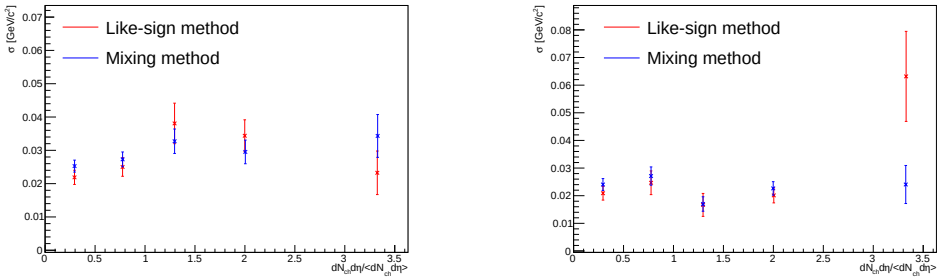

(a) $\rho + \omega$ **(b)** ϕ

Figure 4.12: Mass width as a function of charged-particle multiplicity (BG : VWG)

Chapter 5

Summary

In this study, in order to observe QGP in small systems, I measured two physics with p-p collisions at center-of-mass energy $\sqrt{s}$ =13.6 TeV with updated detector systems in 2022. the one is J/ψ suppression. The charged-particle multiplicity dependence of J/psi production should show slower increasing than linear with increasing of charged-particle multiplicity. The other is restoration of spontaneously chiral symmetry breaking. The $\rho + \omega$ mass width should broad in high charged-particle multiplicity.
As a result, the dependence of self-normalized J/ψ yield on charged-particle multiplicity shows strange behavior at low charged-particle multiplicity. It should behave in such a way that it passes through the origin. The J/ψ yield and the number of events are compared with results of proceeding study. The number of events in this study has weak difference from proceeding study at the low charged-particle multiplicity, whereas large at the high charged-particle multiplicity by a factor of 10^{-1}. J/ψ yield in this study shows significant enhancement at low multiplicity, but its cause is not via yield estimation process. This implies that accuracy of charged-particle multiplicity measurement may be cause and should be investigated more. he mass width of $\rho+\omega$ and ϕ as a function of charged-particle multiplicity show weak dependence of charged-particle multiplicity. The mass width of $\rho + \omega$ and ϕ is higher than PDG values by a factor of 2 for $\rho + \omega$ compared with PDG of ω and 4 for PDG of ϕ due to detector resolution. The ρ mass width in PDG is so high that can be seen if $\rho + \omega$ is separated independently. In case quality of track reconstruction improves more, the mass width of ω and ϕ can be also observed. In this study, the data has a problem of phi angle reconstruction. Reconstructed invariant mass peak is expected to be more

sharp with fixing it and additional track selection. To check the charged-particle multiplicity measurement can make it possible to see yield and mass width as a function of charged-particle multiplicity. The separation between prompt and non-prompt J/ψ is remaining task to see J/ψ suppression.

Acknowledgement

At the first, I appreciate all member of laboratory, family, friends and others who encouraged me in most. I would like to express my sincere gratitude to staffs in quark physics laboratory. Dear Kenta shigaki who is my supervisor, thanks for his guidance and discussion during my laboratory life including analysis and how to built strategy to face issues, I'm able to summarize my study for this thesis. Dear Yorito Yamaguchi, I completed my tasks in CERN MFT DCS on-call shift otherwise there are many problems, and off course my study via mainly help in meeting. Dear Satoshi Yano, not only discussion, but also analysis method and general issues in ALICE are driven. I was able to proceed my analysis with his concrete direction. Dear Masanori Ogino, I am indebted to his help in discussion. He often summarized my message that is hard for me during meeting. Dear Kensuke Honma, all of his comments is surprising for me and unencountered. Dear Takahiro Miyoshi, programming and knowledge of basis of nuclear physics are from him. I am deeply grateful to it.
I wish to extend my appreciation to students in laboratory. Special thanks for Motomi Oya are due to analysis discussion and knowledge to deal with technical problem. I also deeply appreciate comrades in my master life. I was encouraged from them significantly. They inspired me to do my jobs. At the end of this section, I am deeply grateful to all again. Thank you.

Reference

[1] *Particle Data Group, Quantum Chromodynamics*, revised in August 2023.

[2] S. Aoki, K.-I. Ishikawa, N. Ishizuka, T. Izubuchi, D. Kadoh, K. Kanaya, Y. Kuramashi, Y. Namekawa, M. Okawa, Y. Taniguchi, A. Ukawa, N. Ukita, and T. Yoshié. $2 + 1$ flavor lattice qcd toward the physical point. *Phys. Rev. D*, 79:034503, Feb 2009.

[3] *Gauss Center Supercomputing, Numerical Determination of the Phase Diagram of Nuclear Matter*. Copyright: GSI Helmholtzzentrum für Schwerionenforschung GmbH, Darmstadt/Germany.

[4] Paul Romatschke and Ulrike Romatschke. Viscosity information from relativistic nuclear collisions: How perfect is the fluid observed at rhic? *Phys. Rev. Lett.*, 99:172301, Oct 2007.

[5] Evidence from $d + \mathrm{Au}$ measurements for final-state suppression of high-p_T hadrons in $\mathrm{Au} + \mathrm{Au}$ collisions at rhic. *Phys. Rev. Lett.*, 91:072304, Aug 2003.

[6] CMS Colaboration. Observation of prompt j/ψ meson elliptic flow in high-multiplicity ppb collisions at snn=8.16 tev. *Physics Letters B*, 791:172–194, 2019.

[7] ALICE Collaboration. Enhanced production of multi-strange hadrons in high-multiplicity proton–proton collisions. *Nature Phys 13, 535–539*, (2017).

[8] *Multi-Parton Interactions at the LHC*, December 2018.

[9] A. Ortiz Velasquez, P. Christiansen, E. Cuautle Flores, I. A. Maldonado Cervantes, and G. Paić. Color reconnection and flowlike patterns in *pp* collisions. *Phys. Rev. Lett.*, 111:042001, Jul 2013.

[10] S. The ALICE collaboration., Acharya, D Adamová, and et al. Forward rapidity j/ψ production as a function of charged-particle multiplicity in pp collisions at $\sqrt{s}$ = $5.02 and 13 tev. J. High Energ. Phys. 2022, 15, (2022)$.

[11] j/ψ production versus centrality, transverse momentum, andrapidity in Au+ Au collisions at $\sqrt{s_{NN}} = 200$ GeV. *Phys. Rev. Lett.*, 98:232301, Jun 2007.

[12] Volker Koch. Aspects of chiral symmetry. *International Journal of Modern Physics E*, 06(02):203–249, 1997.

[13] W. Weise. Nuclear aspects of chiral symmetry. *Nuclear Physics A*, 553:59–72, 1993.

[14] *CERN Document Server, The CERN accelerator complex*, August 2018. OPEN-PHO-ACCEL-2018-005.

[15] *CERN Accelerating science, ALICE Experiment*, viewed in Jan 2024.

[16] Domenico Colella and for the ALICE Collaboration. Alice its upgrade for lhc run 3: commissioning in the laboratory. *J. Phys.: Conf. Ser. 2374 012058*, 2022.

[17] The ALICE collaboration. Technical design report for the muon forward tracker. Technical report, CERN LHC ; ALICE, Jan 2015.

[18] *CERN Accelerating science, ALICE O2 Project*, May 2018.

[19] S. Adamová D. et al The ALICE collaboration., Acharya. Measurement of ψ (2s) production as a function of charged-particle pseudorapidity density in pp collisions at sqrts = 13 tev and p–pb collisions atsqrts = 8.16 tev with alice at the lhc. *Phys. 2023, 147*, (2023).

[20] The ALICE collaboration. Addendum of the letter of intent for the upgrade of the alice experiment : The muon forward tracker. Technical report, CERN LHC ; ALICE, Aug 2013.

Appendix

J/ψ production models

- Color Glass Condensate (CGC)

Color Glass Condensate (CGC) is a phenomenon where the gluon density inside hadrons increases in relativistic systems, reaching a saturation state. In addition to the components within hadrons, repeated quark-antiquark pair generation and annihilation occur. When hadrons are accelerated, the lifetime of gluons increases, leading to a longer duration of pair generation and a higher parton density. However, as the parton density increases, gluon fusion also occurs, saturating the parton density. This is a common feature in relativistic systems involving hadrons. Consequently, charm pair production through gluon fusion increases. The formation of charmonium from charm pairs is described by the Improved Color Evaporation method (ICEM). ICEM is a model that describes J/psi production within the framework of pQCD. It involves gluon radiation after charm pair production, leading to the formation of charmonium. Color evaporation signifies the transition to a white color during charmonium formation. ICEM is an improved version of the Color Evaporation Model (CEM), incorporating interactions with other partons in addition to gluon radiation. Although the production quantity remains unchanged, it alters the phase-space distribution of the final state. This allows ICEM to explain the momentum distribution ratio between J/psi and Psi(2S), which the traditional CEM model could not.

- 3-Pomeron CGC

3-Pomeron CGC is a model that considers not only double gluon fusion but also higher-order triple gluon fusion.

- Percolation

Percolation is a model based on the assumption that strings have a finite size. Gluon fusion occurs due to geometric overlap, becoming more likely with an increase in gluon density. As a result, the charged-particle multiplicity decreases. On the other hand, J/psi, being a lighter particle, is not affected by gluon fusion, so its yield remains unchanged and is proportional to the number of strings. Therefore, the ratio of J/psi production and charged-particle multiplicity shows an increasing trend.

- Color Precession Percolation (CPP) CPP (Color Precession Percolation)

is a phenomenological model based on p-Pb collisions. It describes pp collisions by normalizing with the number of nucleon collisions. Additionally, it incorporates the effects of mutual boosting at the saturation scale on a more microscopic scale.

Invariant mass reconstructed by event mixing

Invariant mass reconstructed by like-sign and unlike-sign muon pair in mixed events. These distribution are used for combinatorial BG estimation.

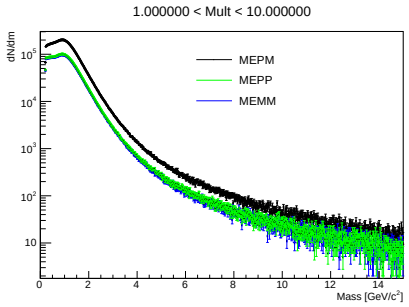

(a) $1 \leq N_{trk} \leq 10$

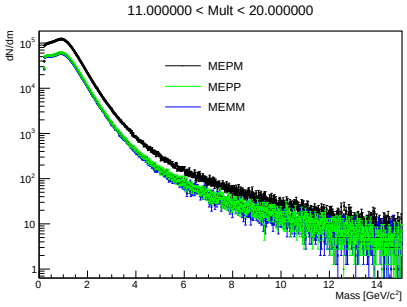

(b) $11 \leq N_{trk} \leq 20$

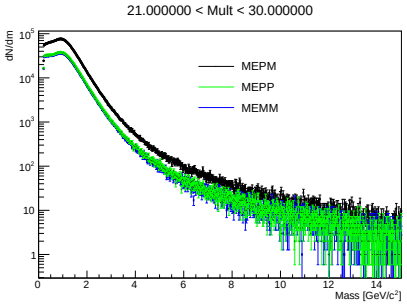

(c) $21 \leq N_{trk} \leq 30$

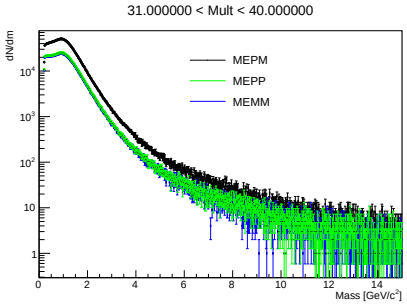

(d) $31 \leq N_{trk} \leq 40$

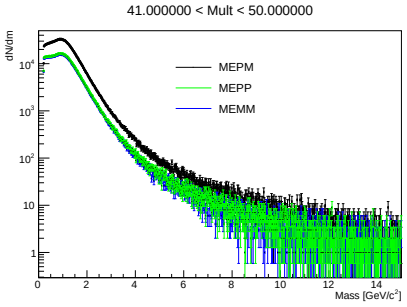

(e) $41 \leq N_{trk} \leq 50$

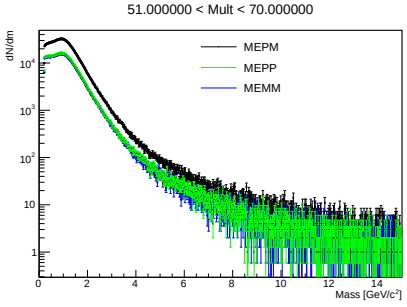

(f) $51 \leq N_{trk} \leq 70$

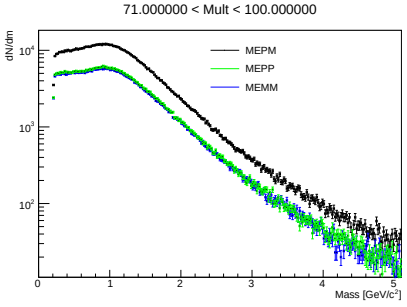

(g) $71 \leq N_{trk} \leq 100$

Figure 5.1: invariant mass reconstructed by muon pair in mixed events

Results : BG functin is single exponential

Low mass vector meson analysis results with single exponential function to estimate remaining BG after combinatorial BG subtraction.

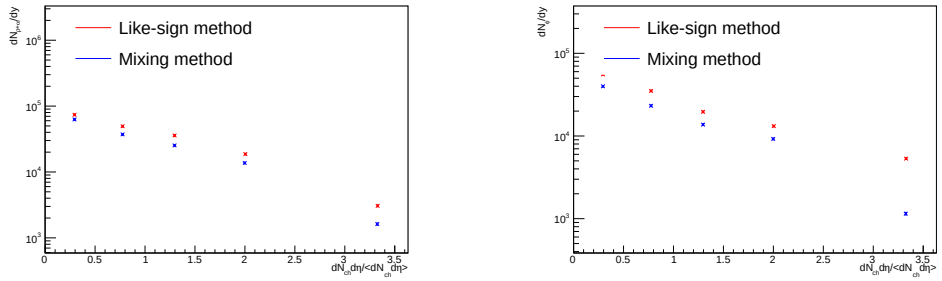

(a) $\rho + \omega$ **(b)** ϕ

Figure 5.2: Row yield as a function of charged-particle multiplicity (BG : exp)

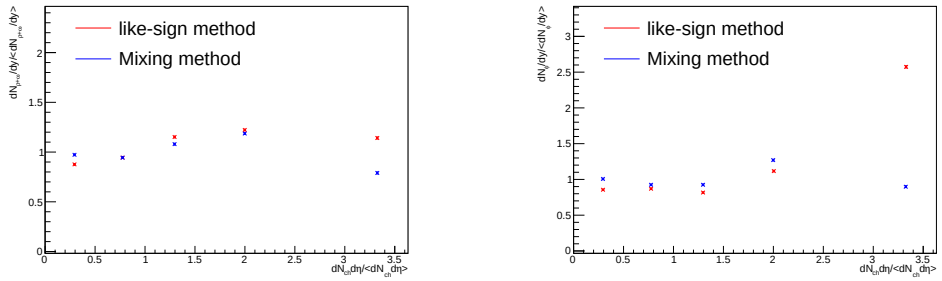

(a) $\rho + \omega$ **(b)** ϕ

Figure 5.3: Self-normalized yield as a function of charged-particle multiplicity (BG : exp)

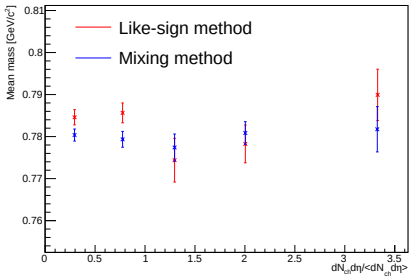

(a) $\rho + \omega$

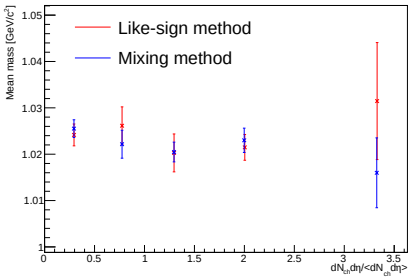

(b) ϕ

Figure 5.4: Mean mass as a function of charged-particle multiplicity (BG : exp)

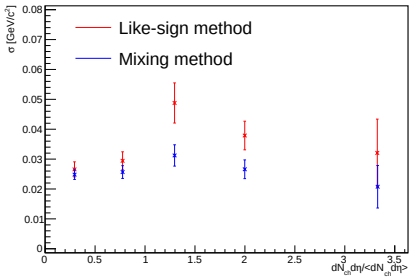

(a) $\rho + \omega$

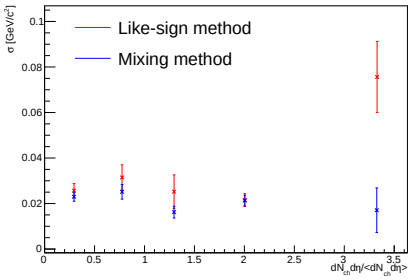

(b) ϕ

Figure 5.5: Mass width as a function of charged-particle multiplicity (BG : exp)